Spatial Buffering of Potassium Ions in Brain Extracellular Space

Kevin C. Chen and Charles Nicholson
Department of Physiology and Neuroscience, New York University Medical School, New York, New York 10016 USA

ABSTRACT It has long been assumed that one important mechanism for the dissipation of local potassium gradients in the brain extracellular space is the so-called spatial buffer, generally associated with glial cells. To date, however, there has been no analytical description of the characteristic patterns of K^+ clearance mediated by such a mechanism. This study reanalyzed a mathematical model of Gardner-Medwin (1983, *J. Physiol. (Lond.).* 335:393–426) that had previously been solved numerically. Under suitable approximations, the transient solutions for the potassium concentrations and the corresponding membrane potentials of glial cells in a finite, parallel domain were derived. The analytic results were substantiated by numerical simulations of a detailed two-compartment model. This simulation explored the dependence of spatial buffer current and extracellular K^+ on the distribution of inward rectifier K^+ channels in the glial endfoot and nonendfoot membranes, the glial geometric length, and the effect of passive KCl uptake. Regarding the glial cells as an equivalent leaky cable, the analyses indicated that a maximum endfoot current occurs when the glial geometric length is equal to the corresponding electrotonic space constant. Consequently, a long glial process is unsuitable for spatial buffering, unless the axial space constant can match the length of the process. Finally, this study discussed whether the spatial buffer mechanism is able to efficiently transport K^+ over distances of more than several glial space constants.

INTRODUCTION

The phenomenon of spatial potassium concentration gradients in extracellular space (ECS) and their buffering by glial cells was first described by Kuffler et al. (1966) and Orkand et al. (1966), who demonstrated that depolarization of glial cells in the leech and the mud puppy was synchronized with neuronal activity. It was hypothesized that the depolarization was mediated by potassium released from spiking neurons. Since then the existence of spatial buffering (SB) has been demonstrated, or at least implied, in numerous experiments (to name a few, Coles and Orkand, 1983; Gardner-Medwin et al., 1981; Gardner-Medwin and Nicholson, 1983; Immel and Steinberg, 1986; Karwoski et al., 1989; Oakley et al., 1992) in various brain regions of vertebrates and invertebrates. Glial cells are interposed between virtually all neurons and axons, with a K^+-dominated resting membrane potential ~20 mV more negative than neurons. The functional roles played by glial cells are far from being understood, but it is generally agreed that their unique membrane properties are involved in the regulation of the extracellular potassium concentration, $[K^+]_o$. The stability of $[K^+]_o$ is essential during prolonged neuronal activity; otherwise there would be uncontrolled variations in neuronal excitability (Barres, 1991; Syková, 1983; Walz, 1989).

In addition to the ubiquitous process of diffusion, at least three different mechanisms are also involved in the clearance of excessive K^+ in the ECS (Amédée et al., 1997; Ballanyi et al., 1987; Coles and Orkand, 1983; Dietzel et al., 1989; Walz, 1989): 1) current-mediated K^+ entry via K^+ channels, especially inward rectifiers; 2) enhanced K^+ transport by Na^+/K^+-ATPase after an increase in intracellular Na^+; and 3) passive KCl uptake through inward rectifier K^+ channels and voltage-gated Cl^- channels. The first mechanism, spatial buffering by K^+ channels, is the focus of this work. When, as a consequence of enhanced neuronal activity, excessive K^+ ions are released into the interstitial clefts, the local $[K^+]_o$ level rises. This causes local depolarization of glial membrane potential that can spread electrotonically through cytoplasm, and possibly gap junctions, to more distal regions. The asymmetrical spatial distribution of potential difference across the glial membrane elicits a local circuit current that, because of the high K^+ permeability, mediates an influx of K^+ into the cell in the region where $[K^+]_o$ is raised, and an efflux of K^+ into the ECS from distal glial processes whose surrounding $[K^+]_o$ is still low. This mechanism of dissipating $[K^+]_o$ spatial gradients in the brain ECS via glial intracellular pathways, termed "spatial buffering" (Orkand et al., 1966), is passive, energy-independent, and in most cases more efficient than diffusion through the interstitium (Gardner-Medwin, 1983a, 1986; Gardner-Medwin and Nicholson, 1983).

Inward rectifier K^+ channels

Many lines of evidence (Kettenmann et al., 1983; Kuffler et al., 1966; Lothman and Somjen, 1975; Newman, 1985, 1993) have confirmed that the glial membrane is selectively permeable to K^+ at rest and passively obeys the Nernst equation over a wide range of $[K^+]_o$ after taking into account the intracellular K^+ activity. Although many voltage-gated channels, previously identified in neurons, have now been found to exist in glia (Barres et al., 1990; Sontheimer, 1994), these channels only contribute a small fraction

Received for publication 6 May 1999 and in final form 29 February 2000.
Address reprint requests to Dr. Charles Nicholson, Department of Physiology and Neuroscience, New York University Medical School, 550 First Ave., New York, NY 10016. Tel.: 212-263-5421; Fax: 212-689-9060; E-mail: charles.nicholson@nyu.edu.

0006-3495/00/06/2776/22 $2.00

of the whole membrane conductance. At least four different voltage-dependent K^+ channels (inward rectifier, Kir; delayed rectifier, Kd; transient A-type, K_A; Ca^{2+}-activated, K_{Ca}) have been identified in glial cells (Sontheimer, 1994). Among them, the dominant K^+ channel is Kir, which retains a high open probability at the resting potential and is easily activated at more negative levels. Kir is known to exhibit an asymmetrical response to hyperpolarization (high conductance) compared to depolarization (low conductance). Therefore K^+ enters the cell more readily than it leaves. The inward rectifier improves the efficiency of SB (Newman, 1993) by enhancing the K^+ influx in regions of elevated $[K^+]_o$ and by spreading the membrane depolarization to more remote parts of the glial cell (Amédée et al., 1997). The hypothesis that the outward rectifier, Kd, facilitates K^+ efflux at depolarized regions during SB, though attractive, is not feasible, except in pathological conditions, because activation requires significant depolarization (-50 mV; Sontheimer, 1994).

Nonuniform Kir distribution and glial endfeet

It has repeatedly been demonstrated (Brew et al., 1986; Newman, 1984, 1985, 1993; Skatchkov et al., 1995, 1999) that glial (Müller) cells in the retina of amphibians have a markedly nonuniform distribution of Kir channels with a predominance at the endfeet regions facing the vitreous humor. The nonuniform distribution of membrane conductance appears to be most effective in directing a large K^+ efflux through the high-conductance region for situations involving distances of only a few space constants (Brew and Attwell, 1985; Eberhardt and Reichenbach, 1987). A refined mechanism, termed "potassium siphoning," was proposed and numerically simulated (Newman, 1993; Odette and Newman, 1988) to show how a specialized endfoot in the Müller cell can direct most K^+ efflux to the vitreous humor. Based on histological evidence, it is highly possible that astrocytes also have regionally specialized K^+ conductance in their multiple processes. Newman (1986) provided further support for this idea, and this led to the conjecture that excessive K^+ in the ECS could be siphoned via astrocytic endfeet processes to regulate blood vessel dilation and cerebral blood flow (Paulson and Newman, 1987). In Schwann cells, Kir is highly localized in the microvilli (Mi et al., 1996), which implies its possible involvement in K^+ regulation in the peripheral nervous system.

Glial syncytium

Many of the in vivo or in vitro experiments involve only a single cell or a few coupled in a syncytium. Thus the geometric length scale in these experiments was no more than 200 μm (the vertical distance of the rather elongated Müller cell in rabbit retina; Reichenbach and Robinson, 1995). To test the effectiveness of the glial syncytium in SB, another type of experiment is required. Such an experiment was devised by Gardner-Medwin (1983a,b) and Gardner-Medwin and Nicholson (1983), who ran the passive SB in reverse by applying an external electrical current across the cerebellum of the rat to evoke a local change in $[K^+]_o$. In other relevant work Dietzel et al. (1982, 1989) measured the field potential changes, caused by the SB K^+ current and cotransport of other ions, across the extent of the cerebral cortex in cats. Because these experiments usually involved hundreds of glial cells, presumably interconnected by gap junctions, the length and time scales in these experiments are, respectively, millimeters and minutes, and any nonuniformity in the distribution of membrane conductance in an individual cell may have been unimportant. This is especially true when the boundary of the tissue is not terminated by glial endfeet. Instead, introducing a statistically averaged membrane conductance, analogous to the tortuosity factor characteristic of the macroscopic structure of the ECS (Nicholson and Syková, 1998), seems more appropriate for understanding the overall SB of a glial syncytial network.

In this paper, we have focused on a macroscopic scale, in the same sense as defined by Gardner-Medwin (1983a,b), by viewing the brain cell microenvironment as a homogeneous continuum and the glial syncytium as an equivalent cable, as shown in Fig. 1. The homogeneous assumption is a necessary simplification when the fate of $[K^+]_o$ within a glial syncytium is simulated. To obtain a practical macroscopic model of K^+ diffusion, a tortuosity factor must be introduced that embodies the macroscopic structure and connectivity of the ECS and neglects differences in the individual properties of the glial cells. Nevertheless, the governing equations and their solutions should also be able to describe a single glial cell, preferably in a cylindrical shape, after a suitable modification of the boundary conditions.

THEORY

In this section we introduce a two-compartment model, consisting of the ECS and the intracellular glial compartment, together with the coupled partial differential equations that govern the temporal and spatial distributions of intra- and extracellular K^+. To estimate how the glial intracellular $[K^+]_i$ varies with $[K^+]_o$, the dynamics of $[Cl^-]_i$ and $[Cl^-]_o$ will be modeled under the assumption of passive KCl uptake, which is considered the most important uptake mechanism for glial cells (Amédée et al., 1997). The $Na^+/K^+/2Cl^-$ cotransporter, the active Na^+/K^+ pump, and the change in ECS volume due to osmotic shifts induced by ionic movement between compartments were not considered here. To do so would require a full accounting of the movement of other ions (such as Na^+) in both compartments and necessitate several other sets of nonlinear differential equations. However, it should be pointed out that the

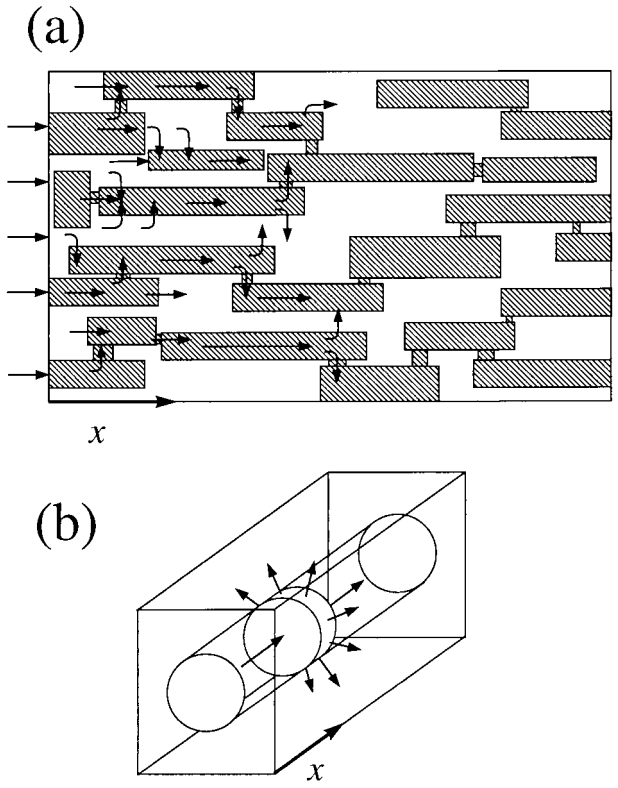

FIGURE 1 (*a*) Schematic drawing showing the simultaneous K^+ transport by spatial buffer (SB) via the glial cells (represented by the shaded rectangles, possibly interconnected by gap junctions) and interstitial diffusion. Arrows indicate K^+ flows due to either diffusion or SB. (*b*) When the macroscopic transport is effectively one-dimensional, the complex intracellular and extracellular geometry in the brain tissue is simplified as a unit rectangular slab, in which an equivalent cylindrical cable represents one single glial cell or a glial syncytium. The rest of the space is composed of neurons and other tissue cells and extracellular space (ECS). For simplicity, neuronal cells were not drawn here. The ECS is regarded as homogeneous with an effective diffusion coefficient D_K/λ_o^2 for potassium. The diameter of the equivalent cable and the size of the slab were arranged to achieve the approximate volume ratio between glial cells and the ECS (α_i:α_o = 0.4:0.2; Dietzel et al., 1989). At both boundaries highly permeable endfeet may be imposed on the cross-sectional area of the glial cylinder. Arrows indicate SB intracellular current and transmembrane K^+ current.

ECS is known to shrink when $[K^+]_o$ is raised well above its resting level (Dietzel et al., 1989; Ransom et al., 1985).

The glial membrane potential $\hat{v}_m$ (mV) is defined as the difference between the intracellular and extracellular potentials, $\hat{v}_i - \hat{v}_o$. Regarding the equivalent cylinder in Fig. 1 as an idealized glial cell, the governing equation for the membrane potential $\hat{v}_m$ of the cylindrical cable at location $\hat{x}$ (m) can be described by conventional cable theory (Gardner-Medwin, 1983b) as

$$\frac{d^2\hat{v}_m}{d\hat{x}^2} = a(r_i + r_o)\hat{i}_m, \tag{1}$$

where $\hat{i}_m$ (A m^{-2}) is the net outward ionic current density across the glial membrane (outward means positive charges move across cell membrane from cytoplasm to ECS) per unit area of glial membrane surface. The averaged glial membrane surface area per unit volume of tissue, available for K^+ exchange, is designated by a (m^{-1}). In Eq. 1, r_i and r_o (Ω m) are the apparent intra- and extracellular resistivity, respectively. (Here r_i and r_o are based on the cross-sectional area of the whole tissue. For the conventional definitions of intracellular and extracellular resistivity, r_i' and r_o', we assumed that $r_i = r_i'\lambda_i^2/\alpha_i$ and $r_o = r_o'\lambda_o^2/\alpha_o$, where α_o, α_i are the volume fractions of the ECS and glial cells in the brain tissue, respectively, and λ_o, λ_i are the tortuosity factors in the corresponding compartments.) Because the typical characteristic time constant of the membrane capacitance is ~1 ms (Newman, 1985), which is too short to be significant in comparison to the typical time scale for diffusion (seconds), the transient term in Eq. 1 has been omitted. We assumed that the transmembrane current $\hat{i}_m$ is strictly carried by K^+ because of the exclusive K^+ permeability of the glial membrane. Furthermore, we expect a negligible contribution to changes in $\hat{i}_m$ to result from the passive entry of Cl^- ions, through independent Cl^- channels.

The K^+ concentration in the extracellular compartment, $\hat{c}_{K,o}$ (moles per unit volume of ECS, mol m^{-3}), is governed by the mass conservation equation in the ECS modified for interactions with the intracellular compartment,

$$\frac{\partial\hat{c}_{K,o}}{\partial\hat{t}} = \frac{a\hat{i}_m}{\alpha_o F} - \frac{\partial\hat{J}_{K,o}}{\partial\hat{x}} - \frac{\alpha_i}{\alpha_o}P, \tag{2}$$

where α_o and α_i (compartmental space per unit tissue volume) are the volume fractions of the ECS and the intracellular space of the glial cells, respectively. The K^+ flux per unit area of the ECS is $\hat{J}_{K,o}$ (mol m^{-2} s^{-1}), and F is the Faraday constant. The term P (mol m^{-2} s^{-1}) represents the net rate of passive influx of KCl into glial cells, following the model of Boyle and Conway (1941). According to this model, a fluctuation in the concentration of K^+ or Cl^- in either compartment will result in a passive KCl redistribution across the membrane, with the final concentrations in both compartments obeying a Donnan equilibrium. The rate of the KCl uptake is assumed to be proportional to the concentration difference,

$$P = \frac{d\hat{c}_{K,i}}{d\hat{t}} = \frac{d\hat{c}_{Cl,i}}{d\hat{t}} = \frac{\hat{c}_{K,i}^{\infty} - \hat{c}_{K,i}}{\hat{\tau}}, \tag{3}$$

in which $\hat{\tau}$(s) is the first-order uptake constant; $\hat{c}_{K,i}$ and $\hat{c}_{Cl,i}$ represent $[K^+]_i$ and $[Cl^-]_i$, respectively; and $\hat{c}_{K,i}^{\infty}$ is the $[K^+]_i$ concentration at Donnan equilibrium, estimated from local K^+ and Cl^- concentrations in both compartments.

Assuming approximately equal mobility for K^+ and other ions (mostly Na^+ and Cl^-) in the ECS, the effective K^+

flux in the ECS is described by the generalized Nernst-Planck equation,

$$\hat{J}_{K,o} = -\frac{D_K}{\lambda_o^2}\left[\frac{\partial \hat{c}_{K,o}}{\partial \hat{x}} + \frac{1}{\Psi}\frac{d\hat{v}_o}{d\hat{x}}\hat{c}_{K,o}\right]. \quad (4)$$

This equation shows that D_K ($m^2\ s^{-1}$), the K^+ diffusion coefficient in the bulk saline, is reduced by the square of the tortuosity factor, λ_o, associated with the ECS (Nicholson and Phillips, 1981; Nicholson and Syková, 1998). The symbol Ψ (mV) designates a standard potential in the units of RT/F (R is the gas coefficient and T is the absolute temperature). The potential driving force in the ECS, $d\hat{v}_o/d\hat{x}$, can be further expressed in terms of $d\hat{v}_m/d\hat{x}$ and the external electric current, $\hat{I}$ ($A\ m^{-2}$), per unit area of the tissue (Gardner-Medwin, 1983b). Additional source/sink terms (such as artificial K^+ injections or extra K^+ released by stimulated neurons) within the domain were not considered in the analysis. These situations will be studied later by numerical simulations.

Transmembrane K^+ flux

The constitutive relation between the transmembrane K^+ current, $\hat{\imath}_m$, and the membrane potential is usually empirical; thus in Gardner-Medwin (1983b) the nonlinear Goldman-Hodgkin-Katz model was employed, whereas here we adopt the simpler Ohm's law,

$$\hat{\imath}_m = g_K \cdot \Delta\hat{v} = g_K \cdot (\hat{v}_m - \hat{e}_K), \quad (5)$$

where $\hat{e}_K$ (mV) is the glial equilibrium potential described by the Nernst equation, $\hat{e}_K = \Psi \ln(\hat{c}_{K,o}/\hat{c}_{K,i})$. The resting potential $\hat{e}_K^o$ (−85.2 mV) is obtained when $\hat{c}_{K,o} = \hat{c}_{K,o}^o$ and $\hat{c}_{K,i} = \hat{c}_{K,i}^o$. The g_K ($S\ m^{-2}$) is the specific glial membrane K^+ conductivity and may vary with many factors. Although various K^+ channels in glial cells are found to be voltage-gated with rectification, ATP-sensitive, or activated by neurotransmitters (see reviews by Barres, 1991; or Walz, 1989) or other cations (mostly intracellular Ca^{2+} or Na^+), we only considered the Kir channel, because of its dominance. Newman (1993) empirically determined the Kir conductivity in retinal Müller cells as

$$g_K = g_K^o \sqrt{\frac{\hat{c}_{K,o}}{\hat{c}_{K,o}^o}}\left\{\frac{1+\exp[18.5/42.4]}{1+\exp[(\Delta\hat{v}+18.5)/42.4]}\right\} \cdot \left\{\frac{1+\exp[-(118.6+\hat{e}_K^o)/44.1]}{1+\exp[-(118.6+\hat{v}_m)/44.1]}\right\} = g_K^o \cdot f_{Kir}, \quad (6)$$

and we adopt his result here. In the above equation, g_K^o is the membrane conductivity at rest ($\hat{c}_{K,o} = \hat{c}_{K,o}^o$, $\hat{v}_m = \hat{e}_K^o$, and $\Delta\hat{v} = 0$). The first term in the parentheses describes how the rectification changes with $\Delta\hat{v}$, and the second term signifies the open channel probability that increases with the membrane potential. For simplicity, the concentration dependence and the two probabilistic functions are lumped together as a rectification factor f_{Kir}. At rest $f_{Kir} = 1$. When the membrane hyperpolarizes ($\Delta\hat{v} < 0$) or $[K^+]_o$ is elevated above the resting value, $f_{Kir} > 1$. In contrast, when depolarization occurs or $[K^+]_o$ is below the resting value, $f_{Kir} < 1$.

Nondimensionalization

To generalize the theoretical as well as the numerical results, it is convenient to express the system of equations in terms of the following dimensionless variables:

$$v = \frac{\hat{v}_m - \hat{e}_K^o}{\Psi}, \quad e_K = \frac{\hat{e}_K - \hat{e}_K^o}{\Psi}, \quad i_m = \frac{\hat{\imath}_m}{\Psi g_K^o},$$

$$x = \frac{\hat{x}}{\Lambda}, \quad t = \frac{D_K}{\lambda_o^2\Lambda^2}\hat{t}, \quad l = \frac{\hat{l}}{\Lambda},$$

$$c_{K,o} = \frac{\hat{c}_{K,o}}{\hat{c}_{K,o}^o}, \quad c_{K,i} = \frac{\hat{c}_{K,i}}{\hat{c}_{K,i}^o}, \quad c_{Cl,o} = \frac{\hat{c}_{Cl,o}}{\hat{c}_{Cl,o}^o},$$

$$c_{Cl,i} = \frac{\hat{c}_{Cl,i}}{\hat{c}_{Cl,i}^o}, \quad c_{K,i}^\infty = \frac{\hat{c}_{K,i}^\infty}{\hat{c}_{K,i}^o},$$

$$I = \frac{r_i r_o}{r_i + r_o}\frac{\hat{I}\Lambda}{\Psi}, \quad \varepsilon_o = \frac{r_o}{r_i + r_o}, \quad \varepsilon_i = \frac{r_i}{r_i + r_o},$$

$$\phi_L = \frac{\alpha_i}{a\Lambda\lambda_i^2}\frac{g_{K,L}^o}{g_K^o}, \quad \phi_R = \frac{\alpha_i}{a\Lambda\lambda_i^2}\frac{g_{K,R}^o}{g_K^o},$$

$$\rho = \frac{\Psi g_K^o a\Lambda^2}{\hat{c}_{K,o}^o \alpha_o F}\frac{\lambda_o^2}{D_K}, \quad \tau = \hat{\tau}\frac{\alpha_o \hat{c}_{K,o}^o}{\alpha_i \hat{c}_{K,i}^o}\frac{D_K}{\lambda_o^2\Lambda^2},$$

in which Λ (m) is the glial electrotonic space constant, defined as $\Lambda = [g_K^o a(r_i + r_o)]^{-1/2}$, $\hat{l}$ (m) is the length of the finite domain, λ_i is the intracellular tortuosity factor within the equivalent glial cable, and $g_{K,L}^o$ and $g_{K,R}^o$ are the basal K^+ conductivity in the left (L) and right (R) endfeet, such that $g_{K,L}^o f_{Kir}$ and $g_{K,R}^o f_{Kir}$ represent the total Kir conductivity of each endfoot, respectively. The endfeet, when present, are represented by the cross-sectional area at the ends of the cylindrical cable in Fig. 1 *b*.

The dimensionless Nernst equation becomes

$$e_K = \ln\frac{c_{K,o}}{c_{K,i}}, \quad (7)$$

and Eqs. 1 and 2 become, respectively,

$$\frac{d^2v}{dx^2} = i_m = f_{Kir}[v - e_K], \quad (8)$$

and

$$\frac{\partial c_{\mathrm{K,o}}}{\partial t} = \underbrace{\rho \frac{\mathrm{d}^2 v}{\mathrm{d}x^2}}_{\mathrm{i}} + \underbrace{\frac{\partial^2 c_{\mathrm{K,o}}}{\partial x^2}}_{\mathrm{ii}} - \underbrace{\varepsilon_{\mathrm{o}} \frac{\mathrm{d}}{\mathrm{d}x}\left(\frac{\mathrm{d}v}{\mathrm{d}x} c_{\mathrm{K,o}}\right)}_{\mathrm{iii}} - \underbrace{I \frac{\partial c_{\mathrm{K,o}}}{\partial x}}_{\mathrm{iv}} - \underbrace{\frac{c^{\infty}_{\mathrm{K,i}} - c_{\mathrm{K,i}}}{\tau / f_{\mathrm{Kir}}}}_{\mathrm{v}}. \tag{9a}$$

Similarly, the governing equation for intracellular $[K^+]_i$ can be written in dimensionless form as

$$\frac{\partial c_{\mathrm{K,i}}}{\partial t} = -\frac{\alpha_{\mathrm{o}}}{\alpha_{\mathrm{i}}} \frac{\hat{c}^{\mathrm{o}}_{\mathrm{K,o}}}{\hat{c}^{\mathrm{o}}_{\mathrm{K,i}}} \underbrace{\rho \frac{\mathrm{d}^2 v}{\mathrm{d}x^2}}_{\mathrm{i}} + \frac{\lambda_{\mathrm{o}}^2}{\lambda_{\mathrm{i}}^2}\left[\underbrace{\frac{\partial^2 c_{\mathrm{K,i}}}{\partial x^2}}_{\mathrm{ii}} + \underbrace{\varepsilon_{\mathrm{i}} \frac{\mathrm{d}}{\mathrm{d}x}\left(\frac{\mathrm{d}v}{\mathrm{d}x} c_{\mathrm{K,i}}\right)}_{\mathrm{iii}} - \underbrace{I \frac{\partial c_{\mathrm{K,i}}}{\partial x}}_{\mathrm{iv}}\right] + \frac{\alpha_{\mathrm{o}}}{\alpha_{\mathrm{i}}} \frac{\hat{c}^{\mathrm{o}}_{\mathrm{K,o}}}{\hat{c}^{\mathrm{o}}_{\mathrm{K,i}}} \underbrace{\frac{c^{\infty}_{\mathrm{K,i}} - c_{\mathrm{K,i}}}{\tau / f_{\mathrm{Kir}}}}_{\mathrm{v}}. \tag{9b}$$

The terms on the right-hand side of Eqs. 9a and 9b respectively indicate contributions from i) SB transmembrane K^+, ii) diffusion, iii) ionic movement driven by SB loop current, iv) externally applied electrical current, and v) KCl uptake. We also modified the uptake pathway, using the same inward rectification property, f_{Kir}; this will cause KCl entry into glial cells to be further enhanced. Because we assumed that the transmembrane current is composed of K^+ and that the only pathway by which Cl^- can enter glial cells is via passive KCl uptake, the governing equations for $[Cl^-]_o$ and $[Cl^-]_i$ can be similarly written as

$$\frac{\partial c_{\mathrm{Cl,o}}}{\partial t} = \frac{D_{\mathrm{Cl}}}{D_{\mathrm{K}}}\left[\underbrace{\frac{\partial^2 c_{\mathrm{Cl,o}}}{\partial x^2}}_{\mathrm{ii}} + \underbrace{\varepsilon_{\mathrm{o}} \frac{\mathrm{d}}{\mathrm{d}x}\left(\frac{\mathrm{d}v}{\mathrm{d}x} c_{\mathrm{Cl,o}}\right)}_{\mathrm{iii}} + \underbrace{I \frac{\partial c_{\mathrm{Cl,o}}}{\partial x}}_{\mathrm{iv}}\right] - \underbrace{\frac{\hat{c}^{\mathrm{o}}_{\mathrm{K,o}}}{\hat{c}^{\mathrm{o}}_{\mathrm{Cl,o}}} \frac{c^{\infty}_{\mathrm{K,i}} - c_{\mathrm{K,i}}}{\tau / f_{\mathrm{Kir}}}}_{\mathrm{v}}, \tag{10a}$$

and

$$\frac{\partial c_{\mathrm{Cl,i}}}{\partial t} = \frac{D_{\mathrm{Cl}} \lambda_{\mathrm{o}}^2}{D_{\mathrm{K}} \lambda_{\mathrm{i}}^2}\left[\underbrace{\frac{\partial^2 c_{\mathrm{Cl,i}}}{\partial x^2}}_{\mathrm{ii}} - \underbrace{\varepsilon_{\mathrm{i}} \frac{\mathrm{d}}{\mathrm{d}x}\left(\frac{\mathrm{d}v}{\mathrm{d}x} c_{\mathrm{Cl,i}}\right)}_{\mathrm{iii}} + \underbrace{I \frac{\partial c_{\mathrm{Cl,i}}}{\partial x}}_{\mathrm{iv}}\right] + \frac{\alpha_{\mathrm{o}}}{\alpha_{\mathrm{i}}} \frac{\hat{c}^{\mathrm{o}}_{\mathrm{K,o}}}{\hat{c}^{\mathrm{o}}_{\mathrm{Cl,i}}} \underbrace{\frac{c^{\infty}_{\mathrm{K,i}} - c_{\mathrm{K,i}}}{\tau / f_{\mathrm{Kir}}}}_{\mathrm{v}}, \tag{10b}$$

with the dimensionless $c_{\mathrm{Cl,o}}$ and $c_{\mathrm{Cl,i}}$ defined as $\hat{c}_{\mathrm{Cl,o}}/\hat{c}^{\mathrm{o}}_{\mathrm{Cl,o}}$ and $\hat{c}_{\mathrm{Cl,i}}/\hat{c}^{\mathrm{o}}_{\mathrm{Cl,i}}$, respectively, and where D_{Cl} is the diffusion coefficient of Cl^- in saline.

The initial conditions are $c_{\mathrm{K,o}}(x, 0) = c_{\mathrm{K,i}}(x, 0) = c_{\mathrm{Cl,o}}(x, 0) = c_{\mathrm{Cl,i}}(x, 0) = 1$ and $v(x, 0) = e_{\mathrm{K}}(x, 0) = 0$. The extracellular $[K^+]_o$ and $[Cl^-]_o$ are assumed to be fixed at $c_{\mathrm{K,o}}(0, t) = c^{\mathrm{L}}_{\mathrm{K,o}}$, $c_{\mathrm{K,o}}(l, t) = c^{\mathrm{R}}_{\mathrm{K,o}}$, and $c_{\mathrm{Cl,o}}(0, t) = c_{\mathrm{Cl,o}}(l, t) = 1$. For the membrane potential v and the intracellular ions, the boundary conditions to be imposed depend upon the nature of the end constraints. From cable theory, the boundary conditions for the membrane potential v can be set up as

$$\frac{\mathrm{d}v}{\mathrm{d}x} = \begin{cases} \phi_{\mathrm{L}} f_{\mathrm{Kir}}[v(0) - e_{\mathrm{K}}(0)] + I, & x = 0, \\ -\phi_{\mathrm{R}} f_{\mathrm{Kir}}[v(l) - e_{\mathrm{K}}(l)] + I, & x = l, \end{cases} \tag{11}$$

where $\mathrm{d}v/\mathrm{d}x$, v, and e_{K} are evaluated at the boundaries, ϕ_{L} and ϕ_{R} are the dimensionless endfoot K^+ conductivities at $x = 0$ and $x = l$, respectively, and $e_{\mathrm{K}}(0)$ and $e_{\mathrm{K}}(l)$ denote the values of e_{K} at $x = 0$ and l, respectively. If ϕ_{L} or ϕ_{R} is nonzero, the corresponding end is also referred to as an open-end boundary. Otherwise it is called a sealed-end boundary. For $c_{\mathrm{K,i}}$, the intracellular electrochemical K^+ flux at the boundaries must be equal to the transmembrane K^+ flux through endfeet, i.e.,

$$\frac{\partial c_{\mathrm{K,i}}}{\partial x} + \varepsilon_{\mathrm{i}} \frac{\mathrm{d}v}{\mathrm{d}x} c_{\mathrm{K,i}} - I c_{\mathrm{K,i}} = \begin{cases} \dfrac{\hat{c}^{\mathrm{o}}_{\mathrm{K,o}} \alpha_{\mathrm{o}} \lambda_{\mathrm{i}}^2}{\hat{c}^{\mathrm{o}}_{\mathrm{K,i}} \alpha_{\mathrm{i}} \lambda_{\mathrm{o}}^2} \rho \phi_{\mathrm{L}} f_{\mathrm{Kir}}[v(0) - e_{\mathrm{K}}(0)], & x = 0, \\ -\dfrac{\hat{c}^{\mathrm{o}}_{\mathrm{K,o}} \alpha_{\mathrm{o}} \lambda_{\mathrm{i}}^2}{\hat{c}^{\mathrm{o}}_{\mathrm{K,i}} \alpha_{\mathrm{i}} \lambda_{\mathrm{o}}^2} \rho \phi_{\mathrm{R}} f_{\mathrm{Kir}}[v(l) - e_{\mathrm{K}}(l)], & x = l. \end{cases} \tag{12}$$

Considering $[Cl^-]_i$, we note that the glial endfeet do not possess particularly large Cl^- conductance; therefore,

$$\frac{\partial c_{\mathrm{Cl,i}}}{\partial x} - \varepsilon_{\mathrm{i}} \frac{\mathrm{d}v}{\mathrm{d}x} c_{\mathrm{Cl,i}} + I c_{\mathrm{Cl,i}} = 0, \quad x = 0, l. \tag{13}$$

Interpretation of dimensionless parameters

Obviously, the two most important dimensionless parameters are Λ and ρ. The space constant Λ estimates how far the glial membrane depolarization can spread axially. Therefore, Λ is defined in terms of the membrane conductivity in the nonendfoot area. There are two alternative interpretations of the increase in the dimensionless length l: it can mean either an actual increase in the glial geometric length $\hat{l}$ or a reduction in the space constant Λ. The parameter ρ represents the relative strength of the SB-mediated K^+ transport compared to the ECS diffusion, measured over a distance of several space constants. The total SB current will be i_{m} multiplied by ρ. However, changing the glial surface area density a or the specific membrane conductiv-

ity g^o_K does not affect ρ because this change will be canceled out by the corresponding modification in Λ^2. Changing ρ without affecting the dimensionless length l is possible only through the effective ECS diffusion coefficient, the ECS volume fraction, or the baseline $[K^+]_o$ level. Therefore, a small ECS volume fraction or a low resting $[K^+]_o$ can boost the SB influence relative to interstitial diffusion. Similarly, a high resting intracellular K^+ concentration minimizes the relative fluctuations of $[K^+]_i$ and hence augments the effectiveness of SB. The low $[K^+]_o$ in the ECS and the high $[K^+]_i$ in glial cells and the selective K^+ permeability make glial cells perfectly qualified for the task of SB (Amédée et al., 1997). The resistance ratios ε_o and ε_i indicate the ease with which ionic movements can be induced in each compartment. In addition to diffusion gradients, ionic flux is driven in part by electrical potentials, represented by the terms 3) and 4) in the above dimensionless governing equations. These current-induced ionic movements can also be expressed in the form of ionic transport numbers (Gardner-Medwin, 1983b).

The parameters ϕ_L, ϕ_R indicate the relative weighting of the membrane conductance at the endfeet to those on the cylindrical cable surface of a unit space constant. For a cylindrical glial cell shape (e.g., the Müller cells in retina), assuming the cell diameter to be d and $\lambda_i = 1$, the specific area density a can be written as $(\hat{l}\pi d/\hat{l}\pi d^2/4)\alpha_i$. Then ϕ_L (or ϕ_R) can be shown to be equal to $\hat{l}[(\pi d^2/4)g^o_{K,L}]/\Lambda[\hat{l}(\pi d)g^o_K] = (\hat{l}/\Lambda)(G^o_{Kef}/G^o_K)$, where G^o_{Kef} and G^o_K are the total membrane K^+ conductances in the endfoot and nonendfoot areas, respectively. Assuming $\hat{l}$ of Müller cells to be approximately the same length as Λ and adopting the known ratio of $G^o_{Kef}/G^o_K \simeq 20$ (Newman, 1985), ϕ_L (or ϕ_R) can be as large as 20.

It should be noted that the dimensionless time t and the spatial axis x are defined relative to the space constant Λ, a parameter that encapsulates the membrane properties of glial cells. This way of defining t and x may make it difficult to compare the distributions of ionic concentrations and membrane potentials in absolute units, but it does make the comparisons in dimensionless forms more meaningful. Very often one is interested in comparing how the $[K^+]_o$ distribution changes subject to changes in a specific membrane property, say, the glial membrane conductivity g^o_K or the intracellular resistivity r_i. Changes in these parameters automatically modify Λ and therefore affect the dimensionless t and x. Assume now two cases with the same $\hat{l}$ but different space constants: one is Λ, regarded as a control, and the other is 2Λ. If we extend the domain of the case with 2Λ to twice its original length, $2\hat{l}$, the two cases will have the same relative decay property for the membrane potential (i.e., we keep the dimensionless x fixed). In evaluating the response to the increased domain length, we must compare the $[K^+]_o$ distribution curve at the time $4\hat{t}$ (i.e., we keep the dimensionless time t fixed) to the corresponding curve of the control case with Λ and $\hat{l}$ at time $\hat{t}$. Without SB, the two cases should produce exactly the same curve when the results are displayed on the relative scales. If SB comes into play, however, the comparisons and evaluation of the buffering effect in this dimensionless situation are more objective (because we have excluded the possible influences from diffusion and the potential decay in the equivalent cable). Further comments on the dimensionless scaling, when results are compared in relative scales, can be found in Gardner-Medwin (1983b).

Membrane potential distribution

If we restrict the problem to a constant membrane conductance, it is possible to obtain an explicit expression for the membrane potential distribution $v(x)$ in terms of an arbitrary Nernst potential distribution $e_K(x)$. Although the effect of Kir will be investigated numerically later, to obtain analytical results, we first consider the case of constant conductivity with $f_{Kir} = 1$. A constant f_{Kir} has been used previously by other investigators (Immel and Steinberg, 1986; Newman and Odette, 1984; Odette and Newman, 1988; Eberhardt and Reichenbach, 1987) studying the clearance of K^+. Because we aim to exploit analytical properties and features of SB, employing a constant g_K is sufficient. Letting $f_{Kir} = 1$, the general solution of Eq. 8, subject to the prescribed boundary conditions in Eq. 11, is given by

$$v(x) = \int_0^l G(x,\xi)e_K(\xi)\mathrm{d}\xi + I\left\{\frac{[\cosh x + \phi_L\sinh x] - [\cosh(x-l) - \phi_R\sinh(x-l)]}{(1+\phi_L\phi_R)\sinh l + (\phi_L+\phi_R)\cosh l}\right\} + \frac{\phi_L e_K(0)[\cosh(x-l) - \phi_R\sinh(x-l) + \phi_R e_K(l)[\cosh x + \phi_L\sinh x]}{(1+\phi_L\phi_R)\sinh l + (\phi_L+\phi_R)\cosh l}, \tag{14}$$

where the Green's function $G(x, \xi)$, in which x is the location of a pulse perturbation and ξ is an independent spatial variable, is defined to be

$$G(x,\xi) = \begin{cases} \dfrac{[\cosh x + \phi_L\sinh x][\cosh(\xi-l) - \phi_R\sinh(\xi-l)]}{(1+\phi_l\phi_R)\sinh l + (\phi_L+\phi_R)\cosh l}, & \xi\in[x,l] \\ \dfrac{[\cosh \xi + \phi_L\sinh \xi][\cosh(x-l) - \phi_R\sinh(x-l)]}{(1+\phi_L\phi_R)\sinh l + (\phi_L+\phi_R)\cosh l}, & \xi\in[0,x]. \end{cases}$$

In Eq. 14, the second term only exists when I is nonzero, and the third term only exists when the open-end boundary condition is used. Equation 14 indicates that the potential $v(x)$ at x is not solely a function of local properties but is also influenced by the extracellular K^+ disturbance far away, with the influence decaying exponentially in terms of some space constant. This solution agrees with the statement made by Gardner-Medwin (1983b) that the membrane

potential v in glial cells will be determined not only by the local extracellular K^+ concentrations, but also by those in neighboring regions. The shape of $G(x, \xi)$ may be better understood graphically in Fig. 2, where the Green's function distributions along ξ at different locations of x are depicted. The distribution shows exponential decays on both sides of the pulse location x. When we consider the endfeet, the influence of a nonzero ϕ_L or ϕ_R penetrates from the boundaries to the inner domain, also exponentially. If l is large enough, the shape of G in the inner domain remains unaffected. This exponential decay in G and the fact that the influence of any perturbations cannot extend beyond a few space constants is characteristic of the passive cable.

Simplified linear analyses

We shall only consider the situation of a domain bounded by two parallel surfaces; practically this can be thought of as a typical brain slice. Assume that a slice of brain tissue with a thickness l is initially perfused in a physiological saline containing K^+ at normal physiological concentration (~3 mM for mammalian brains) at both sides under resting conditions. At time zero, the K^+ concentrations of the perfusates at the two sides are set at two different fixed levels. We are interested in the time courses of various ionic concentrations and membrane potential distributions brought about by the interplay of diffusion and SB. We have already simplified the problem by assuming zero rectification ($f_{Kir} = 1$) and $\varepsilon_o = \varepsilon_i = 0$ to eliminate their associated nonlinear terms. For an analytic solution to be feasible, we limit ourselves to the situation of small K^+ disturbances, i.e., $c_{K,o} \approx 1$, in the ECS such that we can ignore the uptake and linearly expand the logarithmic Nernst potential. It is true that active and passive K^+ uptake into glial cells has been shown to occur during neuronal activity (Ballanyi et al., 1987; Coles and Orkand, 1983; Coles and Tsacopoulos, 1979). However, assuming the $[K^+]_o$ fluctuation is only small and recognizing that $[K^+]_i$ is much higher than $[K^+]_o$, it should be a good enough approximation to ignore the uptake by assuming that $c_{K,i} = 1$ and $c_{Cl,o} = 1$. In reality, the extracellular K^+ level can be as high as $c_{K,o} \approx 4$ (because the ceiling level $[K^+]_o \approx 12$ mM; Syková, 1983) during intense neuronal activity, although this is not commonly seen. This ratio can go even higher under pathological conditions (Syková, 1983). Thus the assumption of a constant $c_{K,i}$ and a linear expansion of the logarithmic term is not always valid. However, the analytical solutions, realizable only after the linear form of $\ln c_{K,o} \approx c_{K,o} - 1$ is adopted, while failing to be quantitatively correct, can still provide useful qualitative information about the behavior of $[K^+]_o$ and SB currents in space and time, and so offer valuable insights into the mechanism of SB. Most importantly, it allows us to arrive at linear governing equations that can be solved analytically. To summarize, we give analytical solutions of the following simplified linear equations:

$$\frac{d^2v}{dx^2} = v - (c_{K,o} - 1), \tag{15}$$

$$\frac{\partial c_{K,o}}{\partial t} = \rho \frac{d^2v}{dx^2} + \frac{\partial^2 c_{K,o}}{\partial x^2}, \tag{16}$$

in which the nondimensional logarithmic Nernst potential, $\ln c_{K,o}$, is replaced by $c_{K,o} - 1$, and only the SB term and the diffusion term (terms i and ii in Eq. 9a) are considered. Comparisons of results that take into account varying $c_{K,i}$, $c_{Cl,i}$, Kir, and the external current I will be studied numerically, using the fully coupled nonlinear equations, later in the paper.

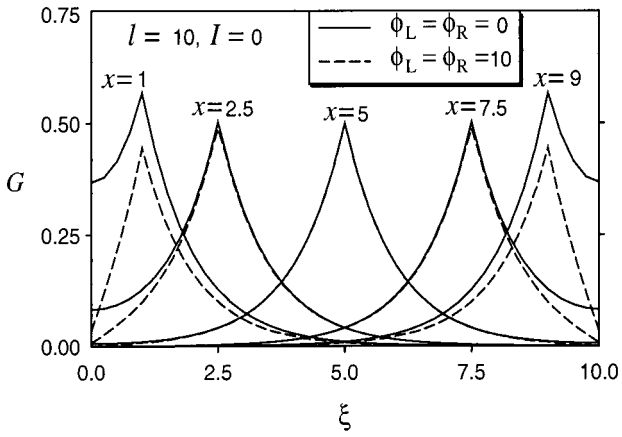

FIGURE 2 Distributions of the Green's function $G(x, \xi)$ along ξ at various pulse locations of x. $G(x, \xi)$ is viewed as a weighting function centered on the K^+ pulse at x for determining the membrane potential distribution. Generally, the distribution G decays exponentially along both sides of the pulse. When the endfoot exists, with elevated conductance, the boundary condition for the membrane potential will be modified, which will also affect the G distribution for the pulse close to the endfeet.

Profiles at steady states

It is possible to achieve a steady state that differs from a uniform distribution as long as the perfusates on both sides act as a stable K^+ source and sink, respectively. Upon letting the left-hand side of Eq. 16 be zero, the steady-state profiles, v^* and $c^*_{K,o}$, of Eqs. 15 and 16 are found to be

$$v^*(x) = \frac{\Delta c_{K,o}}{\sum_i^3 \Theta_i}\{\cosh ux + u\phi_L \sinh ux - [\cosh u(x-l) - u\phi_R \sinh u(x-l)]\} + \frac{\Theta_1}{\sum_i^3 \Theta_i}\left[c^L_{K,o} - \frac{\Delta c_{K,o}}{l}x\right] + \frac{c^L_{K,o}\Theta_2 + c^R_{K,o}\Theta_3}{\sum_i^3 \Theta_i} - 1 \tag{17a}$$

and

$$c^*_{K,o}(x) = -\frac{\rho\Delta c_{K,o}}{\sum_i^3 \Theta_i}\{\cosh ux + u\phi_L \sinh ux - [\cosh u(x-l) - u\phi_R \sinh u(x-l)]\} + \frac{\Theta_1}{\sum_i^3 \Theta_i}\left[c^L_{K,o} - \frac{\Delta c_{K,o}}{l}x\right] + \frac{c^L_{K,o}\Theta_2 + c^R_{K,o}\Theta_3}{\sum_i^3 \Theta_i}, \quad (17b)$$

in which $\Delta c_{K,o} \equiv c^L_{K,o} - c^R_{K,o}$, and u denotes $\sqrt{1+\rho}$. Θ_1, Θ_2, and Θ_3 denote, respectively,

$$\Theta_1 = ul[(1 + u^2\phi_L\phi_R)\sinh ul + u(\phi_L + \phi_R)\cosh ul],$$

$$\Theta_2 = \rho[\cosh ul - 1 + u\phi_L \sinh ul],$$

$$\Theta_3 = \rho[\cosh ul - 1 + u\phi_R \sinh ul].$$

Both solutions consist of two components: the linear component representing the diffusion, and the exponential component representing the effect of SB from the glial core conductor. Because the only source and sink in the domain are assumed to be located at the boundaries, the exponential terms decay toward the inner region. However, if any source/sink appears within the domain, one should expect a corresponding exponential term appearing at the location of each source/sink in the solutions, as justified from the distribution of Green's function shown previously. If $\rho \to 0$, Θ_2 and Θ_3 go to zero but Θ_1 remains finite, reducing $c^*_{K,o}$ to its linear form with the slope $-\Delta c_{K,o}/l$, characteristic of diffusion. If ρ is large, the linear slopes of both $c^*_{K,o}$ and v^* gradually decrease, resulting in the formation of thin boundary layers for $c^*_{K,o}$ at both ends.

The steady-state $[K^+]_o$ distributions, in terms of the dimensionless Nernst potential, together with the membrane potential profiles at various values of ρ, for the sealed-end case ($\phi_L = \phi_R = 0$), are shown in Fig. 3. The profiles of the dimensionless Nernst potential e^*_K (= $\ln c^*_{K,o} = c^*_{K,o} - 1$,

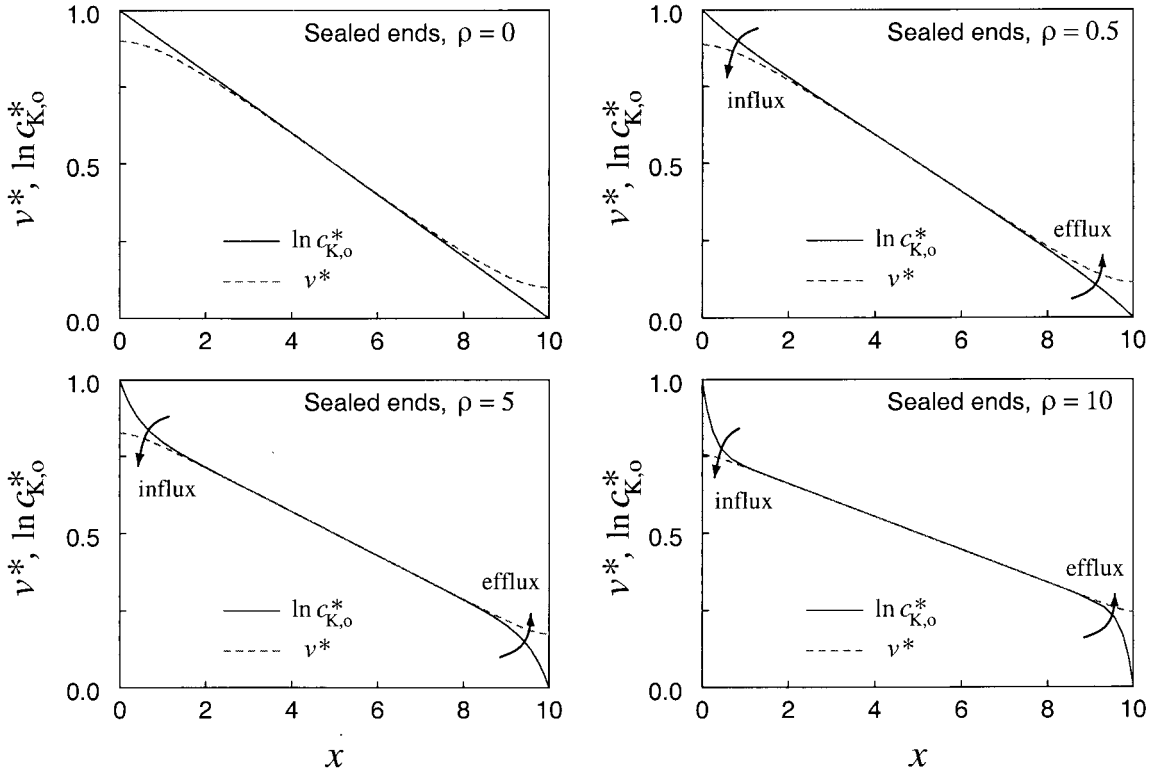

FIGURE 3 Analytical solutions from the simplified linear model (Eqs. 15 and 16): steady-state distributions for the dimensionless Nernst equilibrium potential e^*_K (= $\ln c^*_{K,o}$) (*solid lines*) and the glial membrane potential (*dashed lines*) in a finite domain ($l = 10$). The K^+ source is located at $x = 0$ and the sink at $x = l$. Because in the simplified linear model the e^*_K is approximated by $c_{K,o} - 1$, the solid lines can also represent the ECS K^+ distributions. As the SB strength indicator ρ increases, more K^+ in the ECS is driven into glial cells at the left end (provided by the source at $x = 0$), and an equivalent amount of intracellular K^+ is driven into the ECS at the right end, which then diffuses toward the sink. The transmembrane SB currents at both boundary regions are perpendicular to the axial direction of glial cells. At the center, the diffusion in the ECS and the electrotonic K^+ movement in the intracellular space are parallel to the x axis. The consequence is that the K^+ distribution in the ECS still remains linear in the center (but with a reduced slope) and forms two sharp boundary regions with steep concentration gradients close to both ends.

for the simplified case) and the glial membrane potential v^* differ substantially only in the regions near the boundaries, meaning that the transmembrane current i_m is nearly zero in the interior and SB action mainly takes place in the proximity of the source and the sink. This trend is generally valid regardless of the inclusion of the Kir properties or the varying $[K^+]_i$. In the interior region, the buffering term is negligible because of the small potential driving force, and thus diffusion dominates, resulting in a linear distribution. At the outer regions, enhanced diffusion and SB activity balance each other. As ρ increases, the SB driving force also increases, as indicated by the more significant potential difference in $\ln c^*_{K,o}$ and v^*.

The effect of the relative domain length l on the distributions of $\ln c^*_{K,o}$ and v^* is shown in Fig. 4. Because the dimensionless l is made relative to Λ, a change in the dimensionless l can mean either a change in the geometric dimension representing the glial cells (or the syncytium) or the glial electrotonic space length Λ, due to changes in the membrane K^+ conductance. Thus it is expected that the characteristic thickness of the boundary layers will be independent of the dimensionless l as long as l is far greater than 1. Fig. 4 demonstrates this point by showing that increasing l mainly elongates the interior region, where v^* approaches the Nernst equilibrium potential as l increases.

Fig. 4 also compares the influence of the endfoot conductance on the membrane potential distributions. When the open-end boundary condition with a finite endfoot conductance is used, the endfoot provides an additional pathway

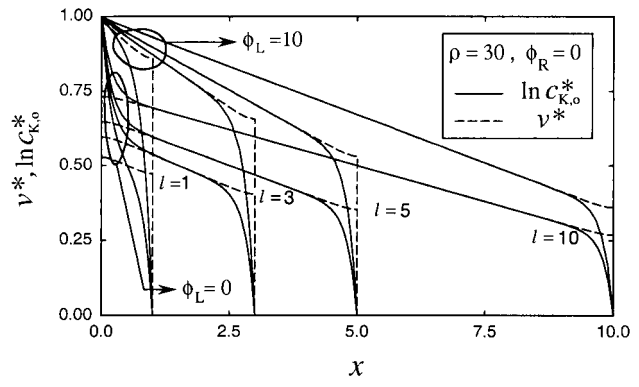

FIGURE 4 Analytical solutions from the simplified linear model (Eqs. 15 and 16): steady-state distributions for the dimensionless Nernst equilibrium potential e^*_K (= $\ln c^*_{K,o}$) (*solid lines*) and the glial membrane potential (*dashed lines*) at different geometric lengths. Even though ρ is large, when a low-resistance endfoot (characterized by a high ϕ_L) is added at the left end, most K^+ is redirected to enter glial cells through this endfoot at $x = 0$, thus reducing the transmembrane current in the nearby nonendfoot area. The diffusion gradient at $x = 0$ therefore becomes smaller. This results in a higher K^+ content in the ECS and a higher membrane depolarization. Both diffusion and endfoot current in the left region are parallel to the x axis. Intracellular K^+ is forced to enter the ECS at the right end, because of the lack of endfeet in that region, and then diffuses toward the sink at $x = l$.

for SB current. This makes the corresponding v^* and $\ln c^*_{K,o}$ in the vicinity of the endfoot conform more completely with each other, thus reducing the transmembrane i_m in the nearby nonendfoot area. It is shown in Fig. 4 that adding an endfoot at the left-end source allows the membrane potential v^* to depolarize more toward its Nernst potential $e^*_{K,o}$ by directing most of the transmembrane K^+ current through the left endfoot. Comparing the curves of the same l with and without an endfoot at $x = 0$, we also see that adding an endfoot facing the source ($x = 0$) brings in more K^+ from the source, thus increasing the $[K^+]_o$ content in the tissue. If the endfoot faces the sink (at $x = l$) instead, more K^+ will be driven out through this endfoot, thus increasing the depletion of the $[K^+]_o$ content. This dependence of SB performance on the endfoot conductance will be further illustrated later.

The K^+ diffusion flux entering/leaving the boundary surface via the ECS pathway at either end can be evaluated by $dc^*_{K,o}/dx$ as $\hat{J}_{K,o}\Lambda\lambda_o^2/(\hat{c}^o_{K,o}\,D_K) = (\Delta c_{K,o}/l)Y$, with Y given by

$$Y = \begin{cases} (1+\rho)(\Theta_1 - \phi_L\Theta_3 l)/\sum_i^3 \Theta_i, & x = 0, \\ (1+\rho)(\Theta_1 - \phi_R\Theta_2 l)/\sum_i^3 \Theta_i, & x = l. \end{cases} \tag{18}$$

If $\rho \to 0$, we have $Y = 1$. Then the overall K^+ flux through the ECS reduces to the expected expression $\Delta c_{K,o}/l$ for pure diffusion, implying that the ratio of the diffusion fluxes with and without SB is simply Y.

The relationship of Y to l, ρ, and endfeet is shown in Fig. 5. Without endfeet ($\phi_L = \phi_R = 0$; Fig. 5 *a*), the diffusion flux ratio Y at the boundary increases with ρ; this increase becomes more significant at a larger l. If an endfoot exists at $x = 0$ ($\phi_L = 5$, but $\phi_R = 0$), the diffusion ratio Y at the same side as the endfoot shows a decreasing trend with ρ at $l \approx 1$ (Fig. 5 *b*), which forms a minimum ECS diffusion ratio along l. This is because at $l \approx 1$ the maximum SB current through the endfoot is achieved, which reduces the corresponding ECS diffusion rate to a minimum. Fig. 5 *c* ($\rho = 5$, $\phi_R = 0$) shows that the ECS diffusion ratio Y measured at $x = 0$ decreases when the endfoot conductivity at the same side (ϕ_L) increases. This decrease in diffusion rate can also be inferred from the slope change of c^* in Fig. 4 when a nonzero ϕ_L is added. The reason for this is that most K^+ flux is redirected through the endfoot entry at the expense of the i_m in the nearby nonendfoot area, which therefore reduces the correspondent ECS diffusion gradient at the entry site. Similarly, a slight minimum along l can be seen around $l \approx 1$. But adding an endfoot at the opposite end (ϕ_R) again eliminates this minimum (Fig. 5 *d*).

To further understand what arrangements (described in terms of ρ, l, ϕ_L, and ϕ_R) are required to achieve the maximum SB activity, we estimated the dimensionless transmembrane $i_m(x)$ to be $v^*(x) - [c^*_{K,o}(x) - 1]$ from Eqs.

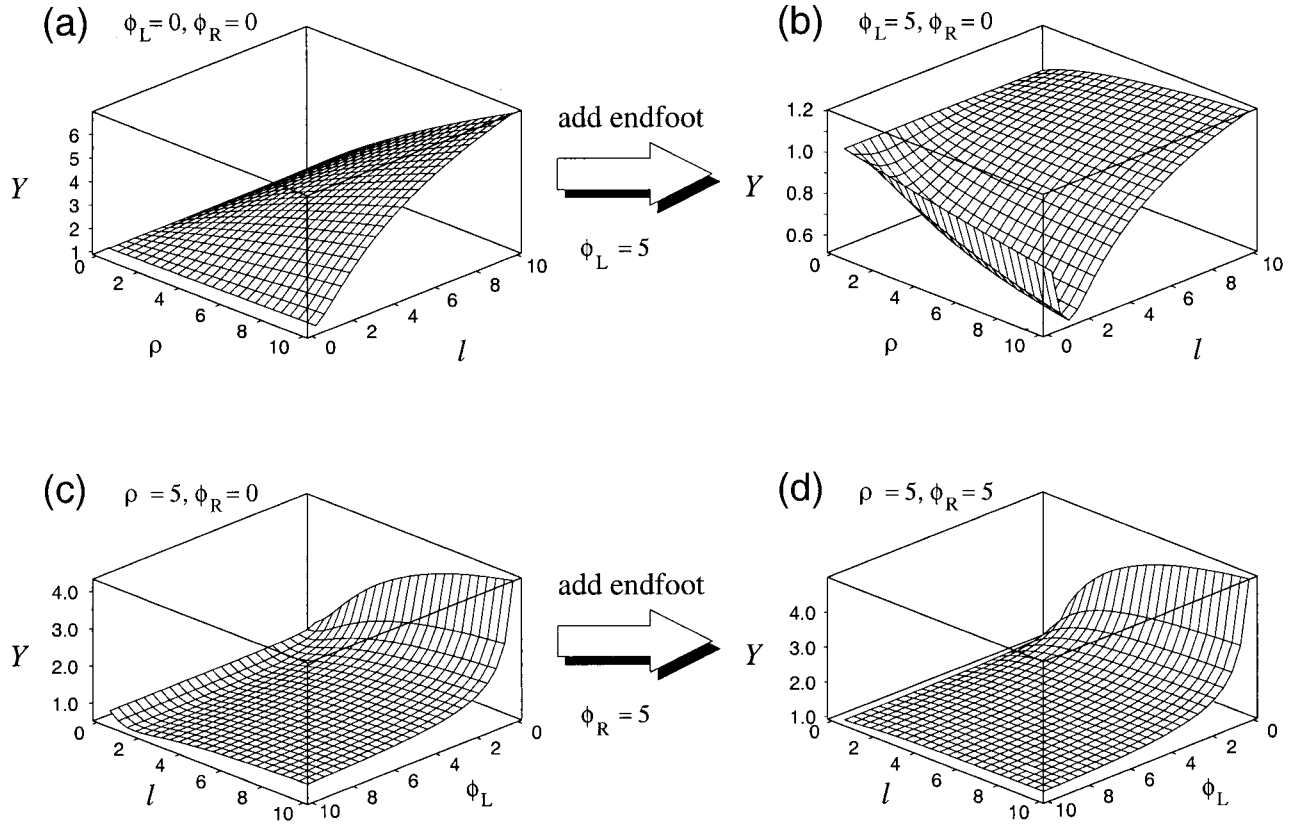

FIGURE 5 Two-dimensional distribution of the steady-state flux ratio Y, estimated by using Eq. 18, as a function of ρ and l (*a* and *b*) or ϕ_L and l (*c* and *d*). Y represents the augmentation factor by which SB augments the K^+ diffusion flux. (*a*) Sealed-end boundaries ($\phi_R = \phi_L = 0$). Y is always larger than or equal to 1 and increases with ρ. For a longer l, the increase becomes almost linear. (*b*) Adding an endfoot at $x = 0$ ($\phi_L = 5$) can produce a minimum point at $l \approx 1$. This point corresponds to the place where the maximum endfoot current occurs. Note that the Y axis scale suddenly drops around 1.0 once ϕ_L is added, and that Y can be less than 1 in the region of $l \leq 1$. (*c*) The diffusion ratio Y decreases with the endfoot conductivity. A smaller diffusion gradient (see Fig. 4) is an indication that most K^+ will be redirected through the endfeet. (*d*) Adding a second endfoot at the far end ($x = l$) removes the minimum at $l \approx 1$ in *c*, but does not change the magnitude of Y very much.

17a and 17b. The overall endfoot current $\hat{i}_{m,e}$, written in dimensionless form as $i_{m,e} = \hat{i}_{m,e}\Lambda/(\hat{c}^o_{K,o}FD_K) = \rho\phi_L i_m(0)$ or $\rho\phi_R i_m(l)$ according to Eq. 12, becomes

$$i_{m,e} = \begin{cases} \phi_L \Delta c_{K,o}(1+\rho)\Theta_3/\sum_i^3 \Theta_i, & x = 0, \\ \phi_R \Delta c_{K,o}(1+\rho)\Theta_2/\sum_i^3 \Theta_i, & x = l. \end{cases} \quad (19)$$

Examining Eq. 19, one can find that as both endfeet ϕ_L and ϕ_R increase to infinity, the endfoot current $i_{m,e}$ approaches the upper limit $\rho(\Delta c_{K,o}/l)$, ρ times as large as the diffusion flux through the ECS pathway (Gardner-Medwin, 1983b). (The extreme of the membrane conductivity is when the membrane barrier ceases to exist, but without losing cytoplasmic constituents to the ECS. That is, only K^+ can freely enter/leave the endfeet membrane, but not other ions.) This limit becomes lower if only one endfoot operates. Remember that Λ was previously defined in terms of the K^+ conductivity on the membrane surface of the equivalent glial cylinder parallel to the x axis (see Fig. 1 *b*) and did not reflect the properties of the perpendicular area of the core conductor at the end, where endfeet are meant to be located. The relative endfeet conductivities ϕ_L and ϕ_R can therefore be set to arbitrary values without altering Λ.

The relationship of the dimensionless endfoot current $i_{m,e}$ at the source end ($x = 0$) with various parameters is plotted in Fig. 6. For the relationship of $i_{m,e}$ with ρ (Fig. 6, *a* and *b*) and ϕ_L (Fig. 6, *c* and *d*), we see that the endfoot current at $x = 0$ increases with ρ, indicating that a large ρ can enhance the endfoot SB, but only increases with ϕ_L to a limiting value, regardless of whether ϕ_R is zero or not. Thus while a larger endfoot conductance ϕ_L will help enhance the endfoot current that passes through it, the effect of ϕ_L can be saturated beyond a certain value (~2). This means that, after reaching the threshold, depositing more K^+ channels on the endfoot will not increase the endfoot current any further. The endfoot current also exhibits a maximum along l at $l \approx 1$, i.e., when the glial axial length $\hat{l}$ is about the same

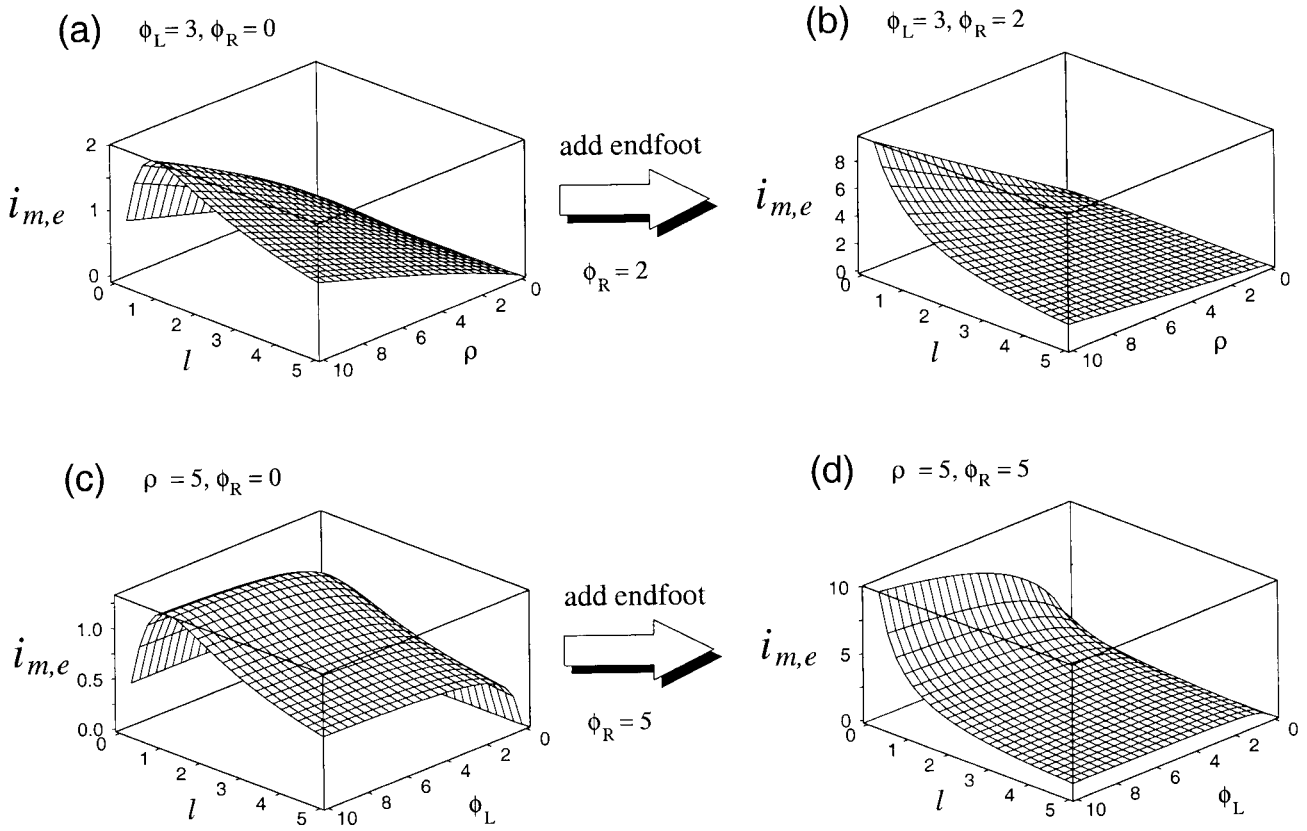

FIGURE 6 Effect of the geometric length l, boundary conditions (endfeet), and SB parameter ρ on the overall dimensionless endfoot current $i_{m,e}$ (estimated by Eq. 19) at steady state. $\Delta c_{K,o} = 1$ was assumed. In *a*, $\phi_L = 3$, $\phi_R = 0$. The overall endfoot current at $x = 0$ is shown to increase with ρ and exhibit a maximum at $l \approx 1$. This local maximum can be removed once a nonzero ϕ_R is added. Notice how the $i_{m,e}$ is magnified in *b* for the region $l \leq 1$. In the distribution of *c*, estimated at $\rho = 5$ and $\phi_R = 0$, $i_{m,e}$ shows a saturation of the endfoot current at large ϕ_L. Similarly, a local maximum exists at $l \approx 1$ and can be removed after a nonzero ϕ_R is added (*d*). Even though, for dual endfeet, a maximum $i_{m,e}$ only exists at $l \approx 0$, notice in *c* and *d* that opening the second low-resistance endfoot at the opposite end ($x = l$) helps to enhance the endfoot current at $x = 0$, especially at shorter l.

size as the space constant Λ. This means that too long a glial process is unable to perform SB efficiently unless the glial cell has a relatively low membrane conductivity g_K^o to match its long process. The model prediction is closely related to the simulation by Eberhardt and Reichenbach (1987), who concluded that the endfoot performance of rabbit retinal Müller cells exhibits a maximum when the Müller cells are of intermediate length (80–100 μm). Existing experimental data indicate that Müller cells have a stalk length of approximately the same order as the length of Λ. However, the endfoot area is overcrowded with K^+ channels, because $\phi_L \approx 20$ for retinal Müller cells and ≈ 10 for astrocytes (Newman, 1985, 1986). These overcrowded endfoot channels do not serve to enhance SB efficiently.

Once ϕ_R at the far end is opened, the location of the maximum endfoot current at $x = 0$ moves to smaller l as ϕ_R increases until the maximum location reaches $l = 0$. This removal of the local maximum currents to $l = 0$ should be attributed to the boundary conditions of $[K^+]_o$, as simulations for the closed ECS system (Fig. 11) did not reveal the same behavior for dual endfeet.

Interpretation of the trends of the dimensionless $i_{m,e}$ defined in Eq. 19 along the dimensionless l should proceed with caution, because the dimensional endfoot current is nondimensionalized with Λ. Thus when studying the trend of $i_{m,e}$ with l, we assume that the dimensional glial geometric length $\hat{l}$ is varied while Λ is kept constant. If one wishes to study the trend of glial endfoot current with g_K^o, which modifies Λ, with a fixed $\hat{l}$, one must multiply $i_{m,e}$ in the above equation by another l ($= \hat{l}/\Lambda$). The multiplication $i_{m,e} \cdot l$ does not show any local maximum along l but increases monotonically with l to a limiting value.

Transient solutions

Equations 15 and 16 were solved next by the method of separation of variables. This method normally yields the solution as the sum of an infinite set of eigenfunctions, each

related to a discrete eigenvalue. The complete solutions can be decomposed into two parts, $c_{K,o}(x, t) = c^{T}_{K,o}(x, t) + c^{*}_{K,o}(x)$ and $v(x, t) = v^{T}(x, t) + v^{*}(x)$, where $c^{T}_{K,o}$ and v^{T} are the transient components for $c_{K,o}$ and v, respectively. The initial and boundary conditions for the transient components are, accordingly,

$$c^{T}_{K,o}(x, 0) = 1 - c^{*}_{K,o}(x), \quad v^{T}(x, 0) = -v^{*}(x) \tag{20a}$$

$$c^{T}_{K,o}(0, t) = 0, \quad \frac{\partial v^{T}}{\partial x}(0, t) = 0 \tag{20b}$$

$$c^{T}_{K,o}(l, t) = 0, \quad \frac{\partial v^{T}}{\partial x}(l, t) = 0. \tag{20c}$$

The analytical derivations of the series solutions are given in the Appendix. The nonlinear, fully coupled governing equations were also solved numerically, using the implicit Crank-Nicholson scheme. The analytical solutions were approximated by truncating the infinite series in Eq. A6 after the first 50 eigenfunctions. We found that the analytical solutions, as derived in Eq. A6 and approximated by the first 50 terms, were in sufficiently good agreement with numerical solutions when the latter were solved under the same assumptions. Because of space limitations, comparisons between analytical and numerical solutions will not be addressed here. Instead, we focus on verifying the qualitative predictions made by the simplified linear model with the numerical solutions from the fully coupled nonlinear differential equations. Values of relevant parameters used in the model are those listed in Table 1 unless otherwise noted. Although parameter values were chosen from different species, those values are not critical to our conclusions, because all simulations were run in dimensionless variables.

First, the transient numerical solutions of $c_{K,o}$ and v from both the simplified linear model and the fully coupled equations were compared in Fig. 7 in terms of the dimensionless glial membrane potentials and the Nernst potentials for the case of $\varepsilon_o = \varepsilon_i = 0$. The resting condition was used initially so that $v(x, 0^-) = 0$ and $c_{K,o}(x, 0^-) = 1$. After $t \geq 0^+$, we set $c_{K,o}(0, t) = 4$ and $c_{K,o}(l, t) = 2$. The logarithmic Nernst potential results in $e_K(0, t) = \ln(4/c_{K,i})$ and $e_K(l, t) = \ln(2/c_{K,i})$, in which $c_{K,i}$ at both cytoplasmic ends must be updated during the simulations. But for the simplified linear model the equilibrium potentials at the boundaries become 3 and 1, respectively. Thus both models are already inconsistent in their magnitudes. However, one can see in Fig. 7, *a* and *c*, that the transient curves from the two models remain similar except in some minor respects. The nonlinear, fully coupled model predicts a transient $c_{K,o}$ curve that takes longer to achieve a steady state compared to the simplified linear model. This is because the nonlinear, fully

TABLE 1 Typical parameter values used in the continuum model and simulations

Parameters	Symbol	Values	References
Apparent extracellular resistivity	r_o	1000 Ω cm*	
Apparent intracellular resistivity	r_i	4000 Ω cm*	
Resting $[K^+]_o$	$\hat{c}^o_{K,o}$	3 mM	Orkand et al. (1966)
Resting $[K^+]_i$	$\hat{c}^o_{K,i}$	73 mM	Kettenmann et al. (1983)
Resting $[Cl^+]_o$	$\hat{c}^o_{Cl,o}$	146 mM	
Resting $[Cl^+]_i$	$\hat{c}^o_{Cl,i}$	6 mM	Ballanyi et al. (1987)
Glial membrane surface density	a	4882 cm^{-1}†	Pilgrim et al. (1982)
Specific K^+ conductivity	g^o_K	1.3×10^{-4} S cm^{-2}	Newman (1985)
Endfoot K^+ conductivity	$g^o_{K,L(R)}$	3.1×10^{-2} S cm^{-2}	Newman (1985)
External electrical current	$\hat{I}$	10–20 μA mm^{-2}	Gardner-Medwin (1983a)
K^+ diffusivity in saline	D_K	2.2×10^{-5} cm^2 s^{-1}	Chung et al. (1999)
Cl^- diffusivity in saline	D_{Cl}	2.4×10^{-5} cm^2 s^{-1}	Chung et al. (1999)
Glial resting (K^+) potential	$\hat{e}^o_K$	−85.2 mV	By Nernst equation
Volume fraction of the ECS	α_o	0.2	Lehmenkühler et al. (1993)
Volume fraction of glial cells	α_i	0.4	Dietzel et al. (1989)
Extracellular tortuosity	λ_o	1.6	Lehmenkühler et al. (1993)
Intracellular tortuosity	λ_i	3.2	Luby-Phelps et al. (1986)
KCl uptake time constant	$\hat{\tau}$	5 s	Newman and Odette (1984)
Faraday constant	F	96,500 Coul mol^{-1}	
Potential unit	Ψ	26.7 mV	Estimated at 31°C

The resting $[K^+]_o$, $[K^+]_i$, $[Cl^-]_o$, and $[Cl^-]_i$ were chosen so that Donnan equilibrium is satisfied. Although all simulations were run with combined parameters in dimensionless forms and did not necessarily adopt the values below, they may be used to obtain an estimate of each dimensionless parameter. According to these dimensional values, we obtained $\Lambda = 0.017$ cm, $\tau = 0.003$, $\rho = 10.73$, $I = 0.5$, $\varepsilon_o = 0.2$, $\varepsilon_i = 0.8$, and one unit of the dimensionless time is ~30 s. For $g^o_{K,L} = 3 \times 10^{-2}$ S cm^{-2}, we obtain a small $\phi_L \simeq 0.1$ because of the large a and λ_i. This small value supports the assumption that in a coupled glial network the endfoot effect is unimportant. For uncoupled cells like Müller cells in retina, the specific area density is probably smaller ($a = 5500$ μm^2 $cell^{-1} \cdot 25 \times 10^6$ cell $cm^{-3} = 1375$ cm^{-1}; Newman, 1993; Odette and Newman, 1988). If we further assume $\lambda_i = 1$ and $\Lambda \sim 70$ μm (Skatchkov et al., 1999), ϕ_L will increase to 9.2. ϕ_L for Müller cells can also be shown to be equal to $(\hat{I}/\Lambda)(G^o_{Kef}/G^o_K) \simeq (70/140)(20/1) = 10$.

*Based on $r'_o = 78.5$ Ω cm and $r'_i = 160$ Ω cm.

†As a result of 1.25×10^5 cm^{-1} (Pilgrim et al., 1982) multiplied by α_i/λ_i^2.

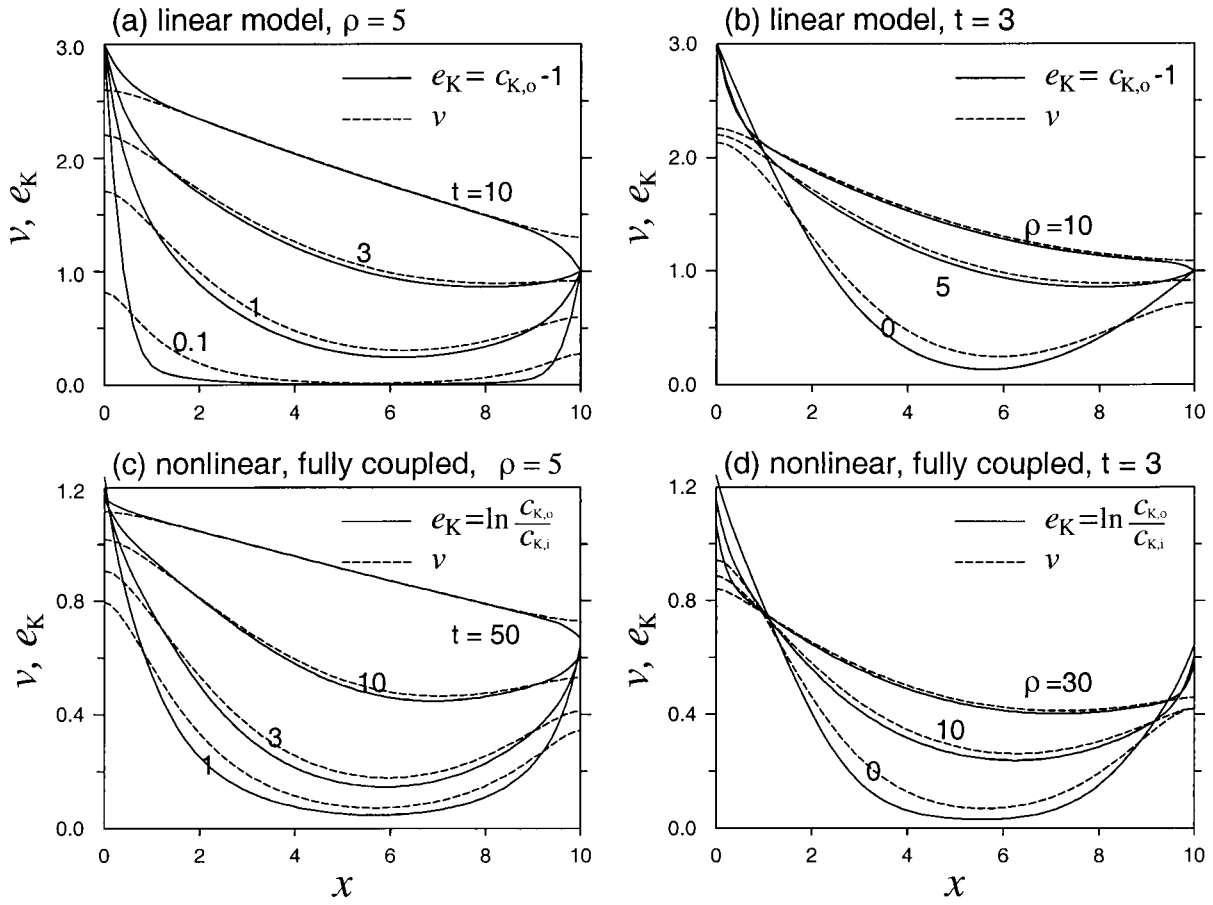

FIGURE 7 Transient solutions of e_K (*solid lines*) and v (*dashed lines*) in a parallel finite domain ($l = 10$). Sealed-end boundary conditions (no endfeet) were assumed, and electrical gradients caused by the SB loop-current were not considered ($\varepsilon_i = \varepsilon_o = 0$); but passive uptake and nonlinear Kir properties were assumed (for nonlinear, fully coupled model only). (*a*) Analytical solutions at different times, using the simplified linear model, which assumes $e_K = c_{K,o} - 1$. (*b*) Snapshot of the solutions at $t = 3$ for different ρ values, showing that increasing ρ accelerates the attainment of steady-state K^+ dynamics. *c* and *d* correspond to *a* and *b*, respectively, for the nonlinear, fully coupled model, which assumes $e_K = \ln(c_{K,o}/c_{K,i})$. The distributions of other ions (e.g., $c_{K,i}$, $c_{Cl,i}$) were not shown here.

coupled model takes into account the KCl uptake, which slows down the equilibrium process. The employment of the asymmetrical Kir channels did not produce significant differences in the profile patterns. Generally, the conclusion that the SB takes place in the proximity of both ends for a sufficiently large t still holds for the fully nonlinear model. Fig. 7, *b* and *d*, depicts the spatial profiles at a fixed time for different buffering strengths ρ. The curves for $\rho = 0$ correspond to a simple diffusion model. As expected, a large ρ expedites the dissipation of K^+ gradients and thus causes the corresponding $[K^+]_o$ profile to reach the steady state faster than does a small ρ.

Because in the previous analytical derivations for the simplified linear model we tacitly neglected the contributions from intracellular ionic concentrations and the electrical gradients in the ionic transport due to the nonlinearity of these factors, it is necessary to determine if such assumptions play a major role in SB. The concentration fluctuations of intracellular ions in our study are caused by 1) the exchanges of ions via the passive uptakes process and 2) the electrical gradient set up by the SB current circuit. The KCl uptake apparently slows down the increase in $[K^+]_o$, a fact that has been known from previous simulations (Gardner-Medwin, 1983b; Odette and Newman, 1988). For the case of $\varepsilon_i = \varepsilon_o = 0$ (the left-hand side of Fig. 8), the accumulation of $[K^+]_i$ and $[Cl^-]_i$ resulting from KCl cotransport is most significant at the two ends, where an elevated $[K^+]_o$ exists initially. K^+ and Cl^- ions enter glial cells through separate channels at $[K^+]_o$-elevated regions and then diffuse intracellularly. It is roughly estimated that raising $[K^+]_o$ from 3 to 12 mM can produce a 16% rise in $[K^+]_i$ in 1 min, which corresponds to a 12 mM local increase in $[K^+]_i$. This 12 mM rise in $[K^+]_i$ is, within a reasonable range, consistent with typical experimental data. For instance, in guinea pig olfactory cortex $[K^+]_i$ changed from 62 to 72 mM in 50 s as $[K^+]_o$ rose from 2.2 to 6.6 mM by stimulation (Ballanyi et

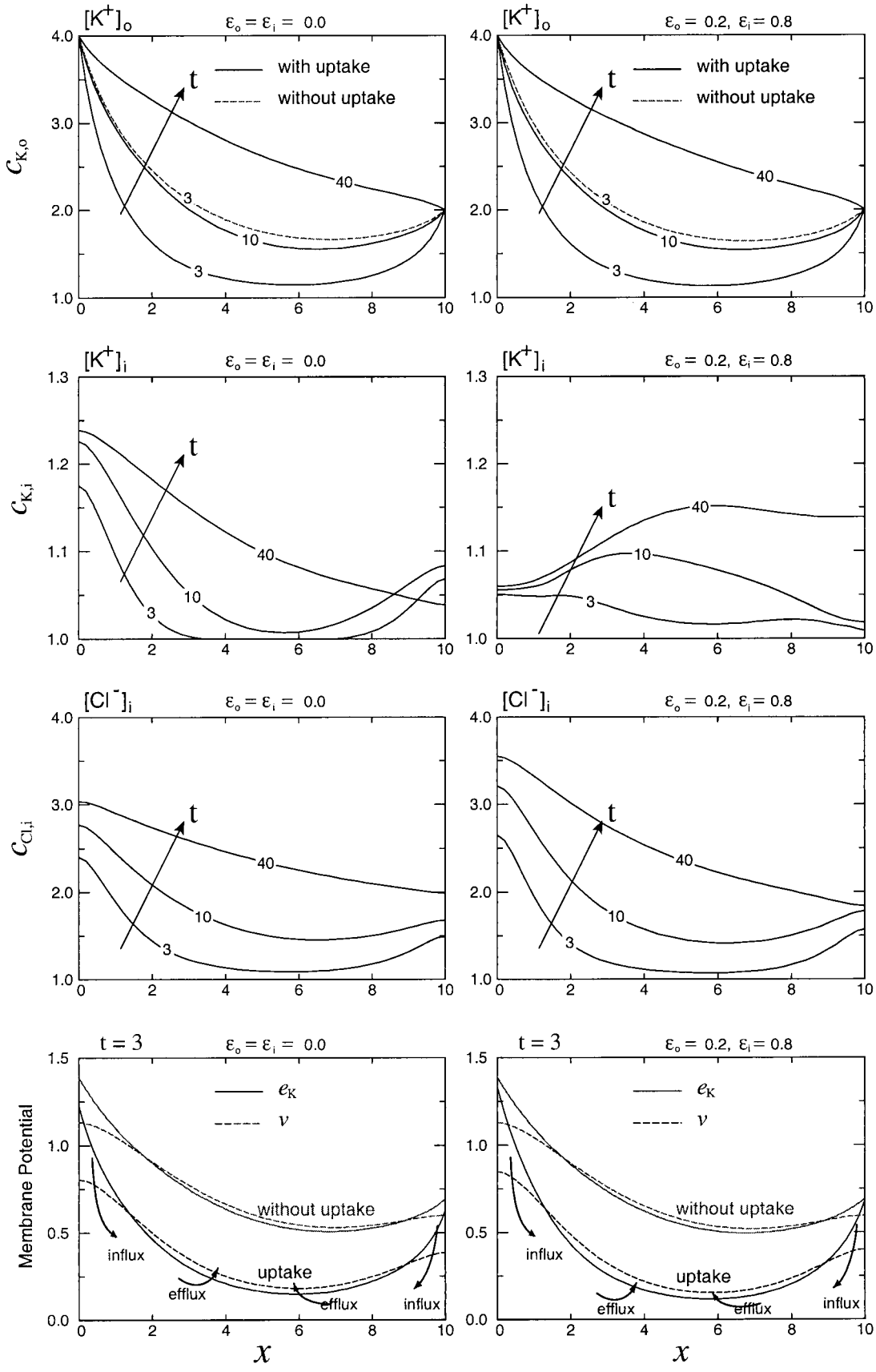
[K+]o
εo = εi = 0.0
εo = 0.2, εi = 0.8
with uptake
without uptake
t
40
3
10
3
cK,o
[K+]i
cK,i
[Cl-]i
cCl,i
t = 3
eK
v
without uptake
uptake
influx
efflux
efflux
influx
Membrane Potential
x

al., 1987). In cultured oligodendrocytes from embryonic mouse spinal cord, $[K^+]_i$ changed from 60 to 69 mM in 2 min as $[K^+]_o$ was raised from 2.2 to 6.6 mM by perfusion (Kettenmann et al., 1983). Because of the low resting $[Cl^-]_i^o$, when an equivalent amount of Cl^- accompanies the K^+ entry it results in a 150% rise in $[Cl^-]_i$.

When the electrical gradient of SB was taken into consideration, as shown on the right-hand side of Fig. 8, it caused little change in the $[K^+]_o$ profiles, but its effect on the axial distributions of $[K^+]_i$ and $[Cl^-]_i$ was very large. Because K^+ is driven with, and Cl^- against, the current, we see that the movement of $[K^+]_i$ is mainly guided by the current direction. Thus $[K^+]_i$ moves toward the sites where K^+ exits, whereas $[Cl^-]_i$ remains at the sites of K^+ entry. This is because generally intracellular resistivity is much higher than the extracellular resistivity. Here we only assumed $r_i/r_o = 4$; values as large as $r_i/r_o = 15$ have also been reported (Gardner-Medwin, 1983b). (Such a high resistivity ratio (15) probably results from the gap junctions in glial coupling, instead of the small volume of the transfer cells as described in Gardner-Medwin (1983b), because the glial volume fraction is unlikely to be below 1% of the total tissue volume.) Thus the nonuniformity of intracellular ionic distributions in our simulations can be viewed as only a modest estimate. Judging from Fig. 8, we conclude that the uptake terms and the nonlinear electrical gradients have a profound influence on the concentration profiles of intracellular ions, although the driving potential difference between e_K and v does not seem to be affected significantly. Therefore, the transmembrane K^+ current remains approximately unchanged. One can imagine that this is because when K^+ is accumulated in glial cells during the phase of elevated $[K^+]_o$, the Nernst equilibrium potential, as estimated by $[K^+]_i$ and $[K^+]_o$, will be lower than that determined without considering net K^+ uptake. However, because the level of the glial membrane potential follows the Nernst potential closely, as is evident from Eqs. 7 and 14, the actual membrane potential also becomes less depolarized. The membrane potential distributions with and without uptake in Fig. 8 reveal such a situation. The consequence of both reduced potentials is then an approximately unchanged current driving force. This conclusion is unaffected whether the uptake process is linear or nonlinear; it is valid as long as the governing equation of the glial membrane potential, Eq. 7, as derived from cable theory, is valid.

The analytical solution assumed no external currents, $I = 0$; therefore we next studied the effect of imposing an external current on the potassium concentration profile. Imagine that a slice of tissue is perfused on both sides with fluid containing a normal physiological potassium concentration. At time $t \geq 0$, a constant electrical current is applied to the tissue. The initial and boundary conditions were chosen to simulate the experiments performed by Gardner-Medwin (1983a) and Gardner-Medwin and Nicholson (1983). No diffusion barrier was assumed on both ends. The simulated dimensionless concentration curves from the nonlinear, fully coupled model were shown in Fig. 9 with a dimensionless $I = -0.5$ (the minus sign means the electrical current enters from the right end of the tissue domain and leaves at the left) at three dimensionless times. The peaks and troughs of the $c_{K,o}$ curves in the upper graph of Fig. 9 occurred as the extracellular K^+ in the right end was driven

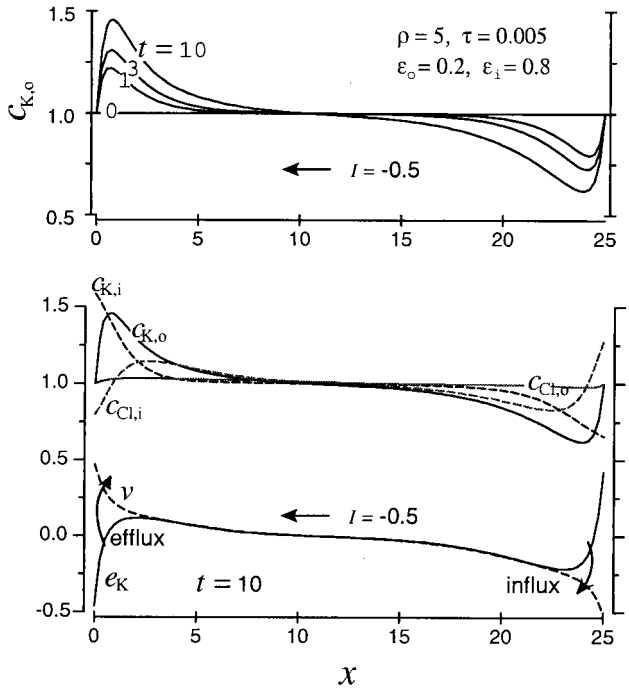

FIGURE 9 Transient profiles of the dimensionless ionic concentrations in both compartments and the membrane potentials evoked by an external electrical current ($I = -0.5$, direction indicated by the *arrow*) at dimensionless $t = 1$, 3, and 10. Sealed-end boundary conditions ($\phi_L = \phi_R = 0$) were used. Simulations considered inward rectification K^+ channels, passive uptake ($\tau = 0.005$), and ionic movement driven by electrical gradients ($\varepsilon_o = 0.2$, $\varepsilon_i = 0.8$). (*Top*) Development of the ECS $[K^+]_o$. (*Bottom*) Distributions of other ions and the membrane potential at $t = 10$.

FIGURE 8 Effect of the passive KCl uptake ($\tau = 0.005$) and the SB-induced electrical gradients in the Nernst-Planck equation on the dimensionless ionic distributions in both compartments. Simulation parameters were $\rho = 5$, $f_{Kir} = 1$. The left panels assumed $\varepsilon_o = \varepsilon_i = 0$. Consequently, the accumulation and distribution of the intracellular ions was due to passive KCl uptake and intracellular diffusion. The right panels assumed $\varepsilon_o = 0.2$, $\varepsilon_i = 0.8$. Consequently, the distributions of the intracellular ions, in addition to the passive KCl uptake and intracellular diffusion, were also driven by the SB-induced electrical gradients described in the Nernst-Planck equation. The transient development of $[K^+]_o$ was slower with uptake than without uptake. While the SB-induced electrical gradient in the intracellular space has a major influence on the distribution of $[K^+]_i$ and $[Cl^-]_i$, the distributions of the extracellular ions are little affected by the inclusion of ε_o. The distribution of the dimensionless $[Cl^-]_o$ was not shown because its distribution is practically flat.

into glial cells and reentered the ECS at the left. The lower graph depicts the distributions of other ions in both compartments and the membrane potentials at a specific time. Interestingly, changes in ionic concentrations were confined to local regions near the boundaries during the initial phase. Even though an external electric field is applied throughout the entire domain, initially the glial membrane potential in the interior region, clamped by the still undisturbed $[K^+]_o$, remains at rest. Only at later times when the concentration changes penetrate into deeper areas does the membrane potential in that region start to depolarize or hyperpolarize. This pattern of development agrees with the conclusions of Gardner-Medwin and Nicholson (1983), who inferred that initially the finite domain can be treated as a semiinfinite domain, and both regions of K^+ aggregation and depletion can be analyzed separately.

The main focus of this paper is to show that the analytical predictions drawn from a simple linear model still remain valid after comparison with models that take more complex factors into account. To confirm this, we ran a series of simulations with varying parametric values to investigate whether the predictions given previously still held qualitatively for a more complex system. This is verified in Fig. 10, which shows an endfoot current behavior similar to that given in Fig. 6. Thus even though the intracellular ionic concentrations ($[K^+]_i$ and $[Cl^-]_i$), the uptake, and the Kir channel properties are taken into account, our conclusions based on the simple linear model are still valid. We also showed how the transient endfoot current evolves in Fig. 10, *c* and *d*. In particular, one sees in Fig. 10 *c* that initially $i_{m,e}$ at $x = 0$ forms a plateau as l increases. Only at a later time is the maximum $i_{m,e}$ around $l \approx 1$ revealed because of the subsidence of $i_{m,e}$ at larger l. This is understandable, considering that a longer domain length l requires a longer time to achieve the steady state.

We note that the situation in Müller cells siphoning the elevated $[K^+]_o$ within the retina predominantly through endfeet to vitreous humor (Odette and Newman, 1988; Newman, 1984, 1985) or astrocytes siphoning elevated $[K^+]_o$ in the ECS to blood vessels (Paulson and Newman,

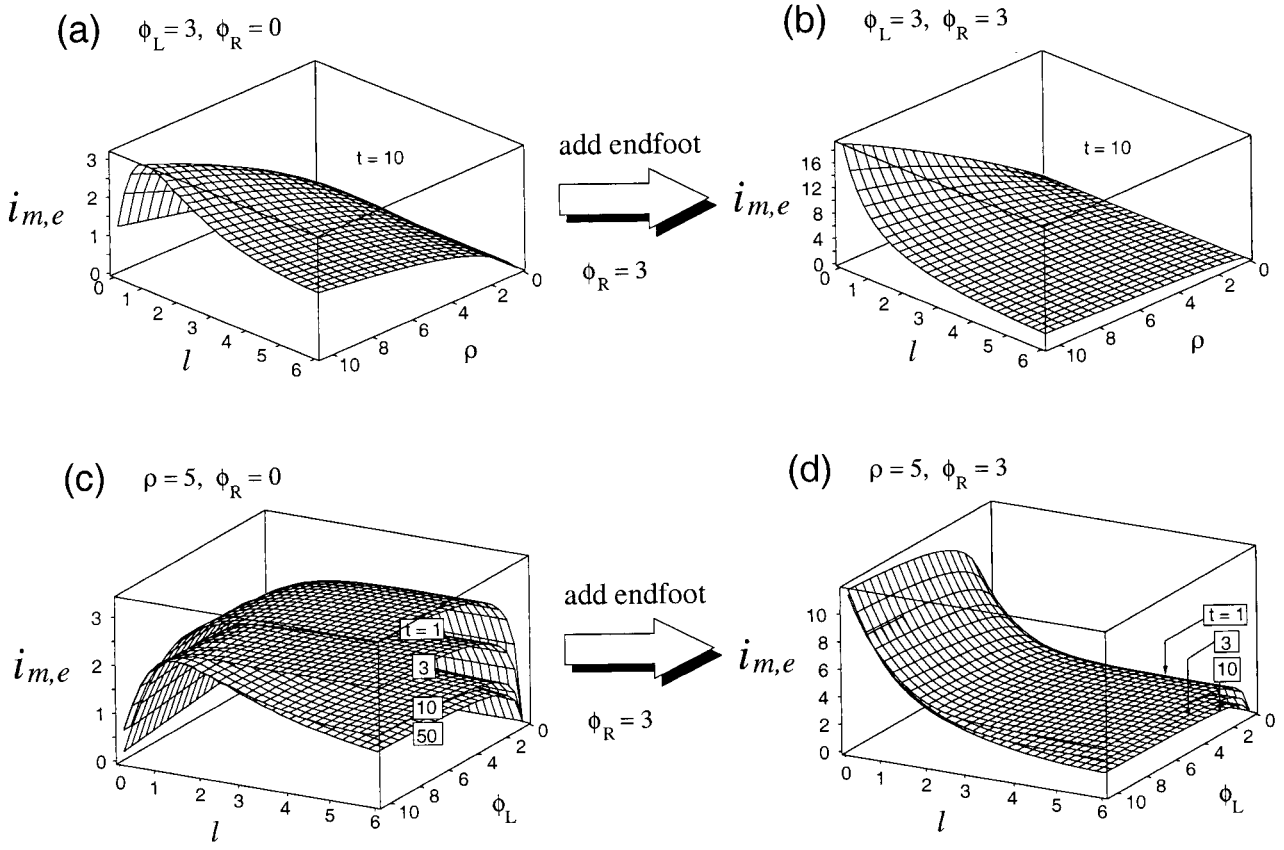

FIGURE 10 Simulation results of the dimensionless endfoot K^+ current based on the nonlinear, fully coupled model, with passive uptake ($\tau = 0.005$), inward rectification channel property, and ionic movement driven by SB-induced electrical gradients ($\varepsilon_o = 0.2$, $\varepsilon_i = 0.8$, but $I = 0$). The dimensionless $i_{m,e}$ at the left endfoot was calculated according to the instantaneous simulated values of the membrane potential, the Nernst potential (from the varying $c_{K,o}$ and $c_{K,i}$ at the left end), and the Kir conductivity (determined by Eq. 6). Some observations: 1) Dual endfeet result in a better endfoot performance (note the different scales for $i_{m,e}$ after ϕ_R is added). 2) In *c*, the local $i_{m,e}$ maximum around $l \approx 1$ does not show initially but becomes evident as time progresses. This endfoot behavior similar to that in Fig. 6 indicates that the simple linear model can be used adequately to infer some basic SB properties.

1987; Newman, 1993) is actually a closed system for the ECS ions. Therefore we modified the boundary condition for the ECS ions ($[K^+]_o$ and $[Cl^-]_o$) into the one similar to Eq. 13 and ran the simulations again. The results are shown in Fig. 11, with a constant point source placed in the center ($x = l/2$) and the K^+ sink at $x < 0$ assumed to be maintained at a resting level. K^+ and Cl^- ions cannot leave the ECS compartment, except for loss of K^+ through the endfoot pathway. As is shown in Fig. 11, this change in boundary conditions for the ECS ions did not alter the existence of the local maximum $i_{m,e}$ at $l \approx 1$. However, we found that in this situation adding another endfoot at the other end ($x = l$) did not remove the local maximum. In addition, in Fig. 11 *c* the $i_{m,e}$ at larger l increases with time, which is the sequence opposite that seen in Fig. 10 *c*. This is because in Fig. 10 the K^+ source was located at the endfoot, but in Fig. 11 the source was away from the endfoot. Therefore, in Fig. 10 a considerable potential driving force existed across the endfoot membrane at the beginning of simulations, and the driving force decreased with time. But in Fig. 11 the endfoot driving force was small initially and built up gradually as the $[K^+]_o$ content near the endfoot rose.

Finally, we investigated the extent to which the Kir properties can boost the buffering efficiency. Newman (1993) compared $[K^+]_o$ dispersion based on inward rectifiers with that arising from ohmic K^+ channels. Our simulations are in general agreement with his results and therefore will not be shown here. However, we found that although, in the presence of the same potential difference, the Kir channels can bring more K^+ into glial cells compared to the nonrectified ohmic channels, the consequence of bringing in more K^+ is to depolarize the membrane further, thus reducing the potential difference across the membrane and the extent of rectification. This tradeoff between depolarization and rectification was noticed by Newman (1993). Only when the local $[K^+]_o$ is high do the advantages of Kir become obvious. When the magnitude of the K^+ dispersion is small, the effect of Kir is not as significant as expected. This is consistent with the findings of Skatchkov et al. (1995) that at physiological $[K^+]_o$ the Kir channels of Müller cells are well suited for carrying K^+ both inward and outward across the membrane.

Comparisons with a former analysis

Brew and Attwell (1985) have analyzed the SB efficiency of Müller cells and found that the best strategy for achieving the optimal SB endfoot current, when the total number of the membrane K^+ channels is fixed, is to distribute the K^+ conductance equally to the endfoot and nonendfoot areas (i.e., $G^o_{Kef} = G^o_K$). Here we found that, given a fixed space constant Λ (or a fixed K^+ conductance per unit membrane surface g^o_K), the maximum endfoot current is achieved when the cell stalk is approximately the same length as Λ. One might ask at this point how our findings (Fig. 11) relate to

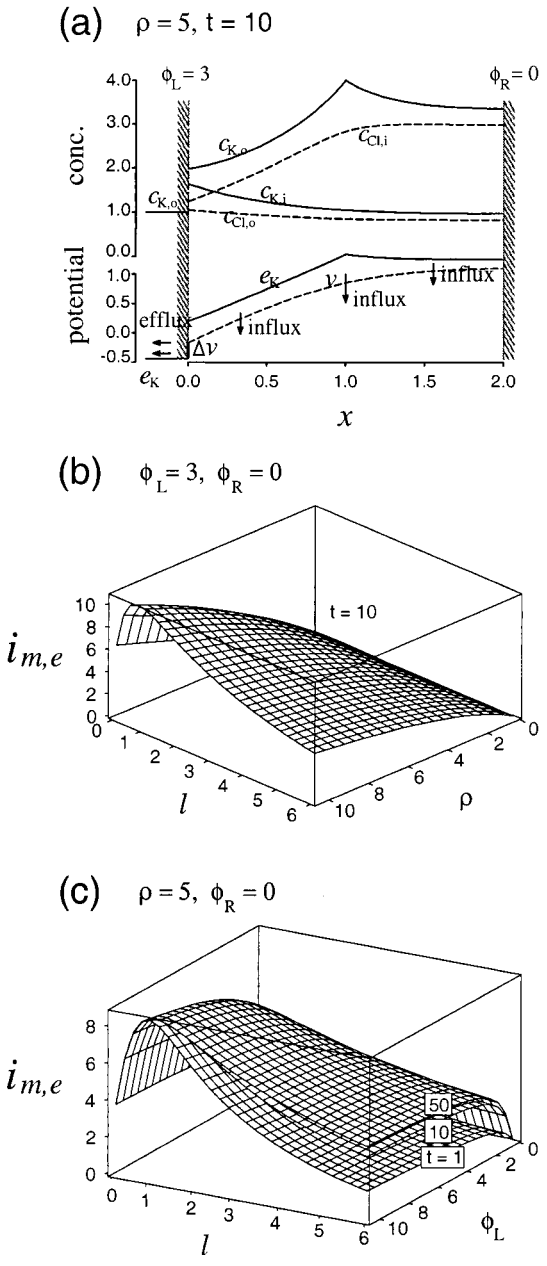

FIGURE 11 Simulations of SB siphoning by Müller cells ($\phi_R = 0$), using the same nonlinear, fully coupled model that incorporated passive uptake ($\tau = 0.005$), inwardly rectifying channels, and ionic movement driven by SB-induced electrical gradients ($\varepsilon_o = 0.2$, $\varepsilon_i = 0.8$, but $I = 0$). The ECS was modified to become a closed system by adopting Eq. 13 as the boundary condition for extracellular ions ($[K^+]_o$ and $[Cl^-]_o$). Thus extracellular K^+ can only leave the domain through the endfoot at $x = 0$. The region in $x < 0$ (vitreous humor) functioned as a steady K^+ sink at rest. A constant K^+ source was placed at the center of the ECS. (*a*) Dimensionless profiles of various ions in both compartments and the membrane potentials. (*b*) Distributions of the dimensionless endfoot $i_{m,e}$ at $x = 0$ versus ρ and l. (*c*) Distributions of the dimensionless endfoot $i_{m,e}$ at $x = 0$ versus ϕ_L and l. Unlike the situation in Fig. 10, adding another endfoot ϕ_R at the right end cannot remove the local maximum at $l \approx 1$ (data not shown here).

theirs, because in our analysis the total membrane conductance is not constant. To show that the two results are essentially the same, the endfoot current used in Brew and Attwell (1985) is expressed, in our notation, as

$$i_{m,e} = \frac{\phi_L (V_{K,o} - V_{Kef})}{1 + \phi_L \dfrac{\cosh l}{\sinh l}}, \tag{21}$$

in which $V_{K,o}$ is the Nernst equilibrium potential, assuming a uniformly elevated $[K^+]_o$ and a constant $[K^+]_i$, and V_{Kef} is the corresponding equilibrium potential at the endfoot side facing the vitreous fluid. Both $V_{K,o}$ and V_{Kef} are assumed to be constant.

The distribution of Eq. 21 versus l and ϕ_L is shown in Fig. 12 *b*. Similarly, we assume in Fig. 12 *b* that Λ is constant when $\hat{l}$ changes. While the $i_{m,e}$ behavior with the relative endfoot conductance ϕ_L is in agreement, the behavior along l shows no local maxima but a monotonic plateau as l increases. This plateau should be attributed to the uniform $[K^+]_o$ in the analysis of Brew and Attwell (1985). From the membrane potential distributions in Fig. 12 *a*, one finds out that the endfoot is mainly siphoning the $[K^+]_o$ in its immediate vicinity. Hence in the ECS next to the endfoot, as more K^+ is siphoned out of the ECS, the $[K^+]_o$ in that region becomes more depleted, and this results in a nonuniform $[K^+]_o$ distribution. One can also see easily that a uniform $[K^+]_o$ distribution cannot satisfy the steady state of Eq. 16, except for $\rho = 0$.

By requiring that the membrane potential and the $[K^+]_o$ distribution must satisfy Eqs. 15 and 16 at steady state, and assuming that a constant K^+ source $V_{K,o}$ is located at the far end of the Müller cell stalk, we rederived the expression for the endfoot current, allowing a nonuniform $[K^+]_o$ distribution at steady state,

$$i_{m,e} = \frac{\phi_L (V_{K,o} - V_{Kef})}{1 + \phi_L Z(\rho)}, \tag{22}$$

in which

$$Z(\rho) = u \frac{\cosh(ul)}{\sinh(ul)} - 4 \frac{\rho}{u^3} \frac{\sinh^2(ul/2)}{\sinh(ul)} + \frac{\rho l}{u^2}, \tag{23}$$

and $u = \sqrt{1 + \rho}$. Apparently when $\rho = 0$, Eq. 22 reverts back to Eq. 21. The distribution given by Eq. 22 versus l and ϕ_L, compared with Eq. 21 in Fig. 12 *b*, once again showed the local maximum at $l \approx 1$. Taking the uniform $[K^+]_o$ distribution as the initial condition, we can say that Eq. 21 describes the $i_{m,e}$ at the beginning of siphoning, and Eq. 22 depicts the $i_{m,e}$ at a longer time. Our computer simulations confirmed that this is the case. For the same driving force $V_{K,o} - V_{Kef}$, the $i_{m,e}$ given by Eq. 22 is much smaller than is predicted by Eq. 21, because at steady states the $[K^+]_o$ content in most regions is smaller than the initial uniform $V_{K,o}$.

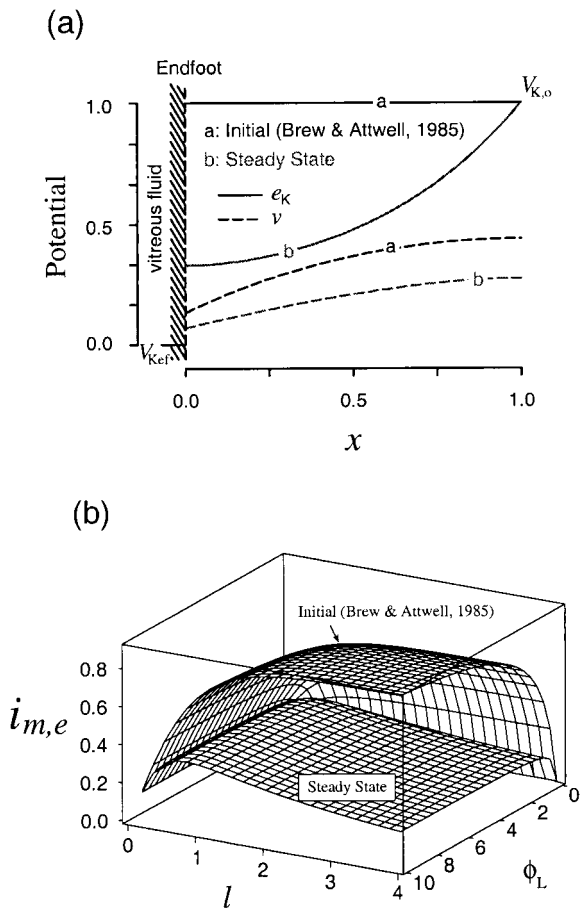

FIGURE 12 Comparisons of the analytical results of the endfoot current in this study with Brew and Attwell (1985). (*a*) dimensionless membrane potentials and the Nernst potentials for a Müller cell of length $l = 1$. The equilibrium potential is $V_{K,o} = 1$ at $x = l$, and at the vitreous humor ($x \leq 0$) $V_{Kef} = 0$. The curves predicted by Brew and Attwell are referred to here as "Initial" because they arose from the initial condition of a uniform $[K^+]_o$ in the ECS. The curves predicted by the present study are referred to as "Steady state" because they take into account the nonuniform $[K^+]_o$ and were derived under steady state. From the distribution of the membrane potentials from Brew and Attwell, we see that closer to the endfoot the potential driving force is greater. Thus the uniform $[K^+]_o$ distribution cannot be maintained indefinitely. For the same $V_{K,o} = 1$ fixed at $x = l$, the K^+ content in the ECS at steady state is bound to be lower than the initial uniformly elevated $[K^+]_o$. This smaller elevation of $[K^+]_o$ near the endfoot results in a smaller potential driving force across the endfoot membrane and, consequently, a smaller endfoot current. (*b*) Distributions of the dimensionless endfoot current predicted from both analyses. The prediction from Brew and Attwell did not show a local maximum around $l \approx 1$, but the prediction based on a nonuniform $[K^+]_o$ did. The much smaller amplitude of our analytical result is due to the smaller $[K^+]_o$ content, as indicated by the smaller potential difference in the potential distribution.

This modification in the endfoot current expression does not alter the required fractional distribution of the total membrane conductance for the optimal SB efficiency (Brew and Attwell, 1985). When the total membrane K^+ conductance is to be preserved, the corresponding endfoot current

expression at steady state is obtained simply by modifying the hyperbolic term in equation 8 of Brew and Attwell with $Z(\rho)$. In Fig. 13 we show how the dimensional endfoot current, given that $\hat{I}$ is fixed, changes along the total K^+ conductance in the endfoot (G^o_{Kef}) and the nonendfoot areas (G^o_K) predicted by both models. The distribution surface was displayed in contour lines of a constant total membrane conductance ($G^o_{Kef} + G^o_K$). Along each contour line, the conductance distribution in the two areas that achieves the optimal endfoot current can be roughly estimated. Also notice that the endfoot current predicted by our model is one order smaller than that given by Brew and Attwell, as explained previously in Fig. 12. The input resistance of intact Müller cells in retina of amphibians is ~8 MΩ (Newman, 1984, 1985), which yields a total membrane conductance of $\sim 1.25 \times 10^{-7}$ S. For such a small value, the two distributions agree with each other in that the optimal endfoot current is obtained at the fraction percentage 50% in the nonendfoot area, and this optimal endfoot current skews gradually toward a larger fraction percentage in the nonendfoot area as the total membrane conductance increases. However, an interesting discrepancy occurs in the region of extremely large membrane conductance. If the total membrane conductance becomes 500-fold larger, as seen from the bottom graph of Fig. 13, the optimal endfoot current from our model ceases to produce a dependence on the conductance fraction as strong as that of Brew and Attwell.

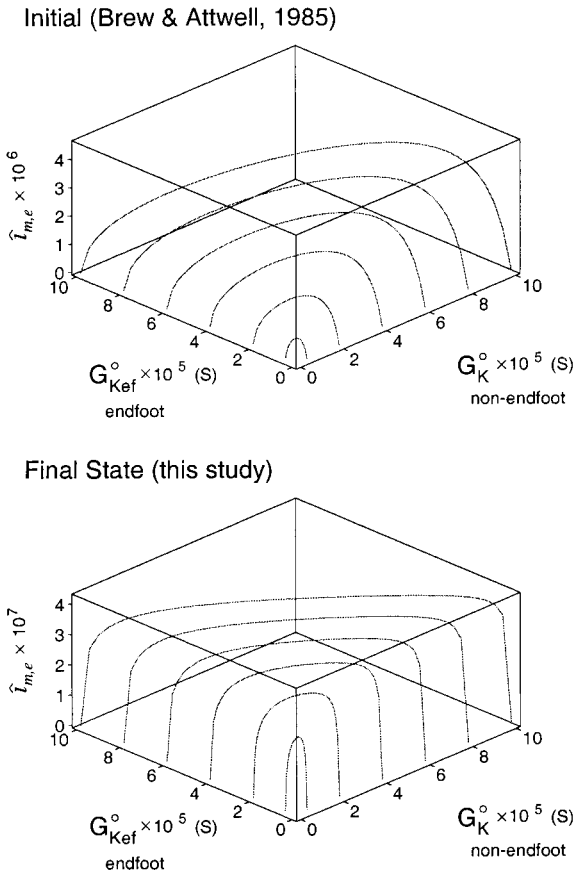

FIGURE 13 The contour line distribution of the dimensional endfoot current versus the total membrane conductance in the endfoot (G^o_{Kef}) and the nonendfoot areas (G^o_K). For comparison purposes, equation 7 of Brew and Attwell (1985) was used, but the hyperbolic term was modified by $Z(\rho)$ (defined in Eq. 23), with the same parameters (intracellular resistance $3.14 \times 10^{10}\ \Omega\ m^{-1}$, cell stalk length 80 μm) in their analysis. The "initial" and "final state" distributions were generated with $\rho = 0$ and $\rho = 5$, respectively. Along each contour line, the total membrane K^+ conductance ($G^o_{Kef} + G^o_K$) is constant. For the total membrane conductance of Müller cells of $\sim 1 \times 10^{-7}$ S, as measured in frog retina by Newman (1984, 1985), the two distributions give the same prediction: an optimal endfoot current obtained at 50% of the total membrane conductance in the nonendfoot area. Differences between the two models appear when the total membrane conductance becomes at least 100-fold larger; our model predicts an almost flat distribution between G^o_K and G^o_K, although the optimal point of the contour line still skews toward the G^o_K side. However, if a larger $\hat{I}$ or ρ is used, this flat distribution starts to appear earlier at a smaller total membrane conductance.

CONCLUSIONS

We developed a one-dimensional continuum model for K^+ transport in the brain ECS. The mechanisms considered here include passive KCl uptake, interstitial diffusion, and spatial buffering through glial intracellular pathways. In an attempt to analyze the distributions of $[K^+]_o$ and the glial membrane potential, a simplified linear model was derived. This model revealed that the maximum endfoot current occurs when the glial geometric length is approximately equal to the electrotonic space constant along the nonendfoot glial cable. This conclusion was subsequently verified to hold true, even when many other factors that were not included in the simple linear model were taken into account. This suggests that the basic SB properties can be inferred directly from linear cable theory. We compared our analytical results with those of Brew and Attwell (1985) for the optimal SB siphoning of Müller cells and found that their results did not exhibit the local maximum at $l \approx 1$ because Brew and Attwell assumed a uniformly elevated $[K^+]_o$ in the ECS. We showed that, after allowing the K^+ distribution in the ECS to be nonuniform, this local maximum can be revealed. This conclusion about the local maximum, although derived from a steady state with a specific arrangement in the K^+ source, is not restricted to these conditions. Any SB operation after a period of time should automatically produce such a local maximum. This point is supported by the transient evolution of the endfoot current shown in Fig. 11, in which a point K^+ source was used.

A still unresolved question about glial membrane properties is the function of the large endfoot conductance. The highly asymmetrical distribution of membrane K^+ conductance in Müller cells (95% in endfoot and 5% in others; Newman, 1984) cannot siphon K^+ optimally from the ECS to the vitreous humor (Brew and Attwell, 1985). This is especially true because the Müller cell has only one endfoot

process. However, the present analysis has shown that the advantage of the extremely large endfoot conductance can be most evident if more than one endfoot operates simultaneously over a short distance. Astrocytes that possess multiple processes and terminate in proximity to capillaries or pial surfaces appear to fit in this requirement. Paulson and Newman (1987) hypothesized that astrocytes regulate the dilation of blood capillaries through K^+ released from the glial endfeet abutting the blood vessels. Although the conjecture concerning vascular regulation has failed to receive experimental support, it remains plausible that endfeet can deliver K^+ into the vicinity of blood vessels. If dual endfeet were considered and the endfeet conductance was sufficiently large compared to the nonendfoot area, K^+ that entered from one endfoot would exclusively exit at the other. This operation could have a higher efficiency if the K^+ channels in the nonendfoot area were sparse or the stalk was short. However, evidence is lacking as to whether one of the functions of the high-conductance endfeet in astrocytes (Newman, 1986) is to mediate signal transmission between nearby capillaries. In summary, spatial buffering, as constrained by the leaky cable properties, does not appear to be able to operate over long distances unless some currently unknown factors are involved.

Finally, because of the omission of many mechanisms and other simplifications made in the model, this work was not intended to be quantitatively accurate in describing what has been observed under normal physiological conditions. In particular, the effect of the Na^+-K^+ electrogenic pump has been neglected in this study but is believed to exert a substantial influence over longer times in restoring the homeostasis of $[K^+]_o$ (Amédée et al., 1997; Ballanyi et al., 1987; Coles and Orkand, 1983). Also neglected has been the change in the ECS volume due to water movement when extensive ion exchange between compartments occurs. However, we suspect that including such factors will not alter our main conclusion substantially. Our philosophy has been that, while it is possible to run a complete simulation that includes other known mechanisms, an analytical solution remains preferable for revealing the underlying aspects of spatial buffering. The type of analysis presented here provides a qualitative dissection of the SB mechanism for K^+ transport and can provide new insights into the role of glial cells in K^+ homeostasis.

APPENDIX A: TRANSIENT SOLUTIONS IN PARALLEL DOMAIN

Because of the homogeneous boundary conditions for v^T, we can write $c^T_{K,o}(x, t)$ and $v^T(x, t)$ in the following separable forms:

$$c^T_{K,o}(x, t) = \sum_{n=1}^{\infty} \Gamma_n(t) \cdot C_n(x), \quad v^T(x, t) = \sum_{n=1}^{\infty} \Gamma_n(t) \cdot V_n(x), \tag{A1}$$

in which n is an integer suffix. Assuming $\varepsilon_o = \varepsilon_i = 0$ and $I = 0$, substituting Eq. A1 into Eqs. 15 and 16 yields a set of eigenfunction problems. For the spatial part, we substituted in $C_n = V_n - d^2V_n/dx^2$ and solved a fourth-order differential equation for V_n. The $C_n(x)$ and $V_n(x)$ satisfying the homogeneous boundary conditions were thus obtained, with $C_n(x)$ in the form of

$$C_n(x) = \chi_n[e^{\sqrt{a_n+b_n}(x-l)} - (-1)^n e^{-\sqrt{a_n+b_n}x}] + \chi_n P_n \cos(\sqrt{b_n - a_n}x) - Q_n \sin(\sqrt{b_n - a_n}x), \tag{A2}$$

in which $P_n = [(-1)^n - e^{-\sqrt{a_n+b_n}l}]$, $Q_n = [(-1)^n + e^{-\sqrt{a_n+b_n}l}]$, χ_n denotes

$$\chi_n = \frac{1 - (a_n + b_n)}{1 + (b_n - a_n)} \cdot \sqrt{\frac{b_n - a_n}{a_n + b_n}}, \tag{A3}$$

and a_n and b_n denote

$$a_n = \frac{1}{2}(1 + \rho - \lambda_n) \quad \text{and} \quad b_n = \frac{1}{2}\sqrt{(1 + \rho - \lambda_n)^2 + 4\lambda_n}, \tag{A4}$$

where λ_n is the nth smallest nonzero eigenvalue for the temporal part $\Gamma_n(t) = \exp(-\lambda_n t)$. The discrete λ_n is required to simultaneously satisfy

$$\sin(\sqrt{b_n - a_n}l) = (-1)^n \frac{2P_nQ_n}{\chi_n P_n^2 + Q_n^2/\chi_n} \tag{A5a}$$

and

$$\cos(\sqrt{b_n - a_n}l) = -(-1)^n \frac{\chi_n P_n^2 - Q_n^2/\chi_n}{\chi_n P_n^2 + Q_n^2/\chi_n}. \tag{A5b}$$

The complete transient solution is the sum of the infinite series

$$c^T_{K,o}(x, t) = \sum_{n=1}^{\infty} \mathcal{B}_n e^{-\lambda_n t} C_n(x). \tag{A6}$$

The orthogonality of C_n can be proved by showing that the spatial part of Eq. 16 with the homogeneous boundary conditions is of a Sturm-Liouville type (Carslaw and Jaeger, 1959). $\mathcal{B}_n$ can thus be determined from the initial condition as

$$\mathcal{B}_n = -\int_0^l C_n(x)[c^*_{K,o}(x) - 1]dx \Big/ \int_0^l [C_n(x)]^2 dx. \tag{A7}$$

Because the analytical expressions of the above two integrals are quite lengthy, only the case for $\phi_L = \phi_R = 0$ is shown here:

$$\int_0^l C_n(x)[c^*_{K,o}(x) - 1]dx = -\frac{2b_n[(c^L_{K,o} - 1) - (-1)^n(c^R_{K,o} - 1)]}{(1 + b_n - a_n)\sqrt{\lambda_n(a_n + b_n)}} Q_n, \tag{A8}$$

and

$$\int_0^l [C_n(x)]^2 dx = \frac{b_n(1+\lambda_n)l}{(1+b_n-a_n)^2(a_n+b_n)} Q_n^2 + (-1)^n 4l\chi_n^2 e^{-\sqrt{a_n+b_n}l} - 2\frac{(1-a_n-b_n)[b_n-2\lambda_n]}{(1+b_n-a_n)^2(a_n+b_n)^{3/2}} P_n Q_n. \quad \text{(A9)}$$

This research is supported by National Institutes of Health grant NS 28642 from the National Institute of Neurological Disorders and Stroke.

REFERENCES

Amédée, T., A. Robert, and J. A. Coles. 1997. Potassium homeostasis and glial energy metabolism. *Glia.* 21:46–55.

Ballanyi, K., P. Grafe, and G. ten Bruggencate. 1987. Ion activities and potassium uptake mechanisms of glial cells in guinea-pig olfactory cortex slices. *J. Physiol. (Lond.).* 382:159–174.

Barres, B. A. 1991. New roles for glial. *J. Neurosci.* 11:3685–3694.

Barres, B. A., L. L. Y. Chun, and D. P. Corey. 1990. Ion channels in vertebrate glia. *Annu. Rev. Neurosci.* 13:441–474.

Boyle, P. J., and E. J. Conway. 1941. Potassium accumulation in muscle and associated changes. *J. Physiol. (Lond.).* 100:1–63.

Brew, H., and W. Attwell. 1985. Is the potassium channel distribution in glial cells optimal for spatial buffering of potassium? *Biophys. J.* 48:843–847.

Brew, H., P. T. Gary, P. Mobbs, and W. Attwell. 1986. Endfeet of retinal glial cells have higher densities of ions channel that mediate K^+ buffering. *Nature.* 324:466–468.

Carslaw, H. S., and J. C. Jaeger. 1959. Conduction of Heat in Solids. Oxford University Press, New York.

Chung, S. H., T. W. Allen, M. Hoyles, and S. Kuyucak. 1999. Permeation of ions across the potassium channel: Brownian dynamics studies. *Biophys. J.* 77:2517–2533.

Coles, J. A., and R. K. Orkand. 1983. Modification of potassium movement through the retina of the drone by glial uptake. *J. Physiol. (Lond.).* 340:157–174.

Coles, J. A., and M. Tsacopoulos. 1979. Potassium activity in photoreceptors, glial cells and extracellular space in the drone retina: changes during photostimulation. *J. Physiol. (Lond.).* 290:525–549.

Dietzel, I., U. Heinemann, G. Hofmeier, and H. D. Lux. 1982. Stimulus-induced changes in extracellular Na^+ and Cl^- concentration in relation to changes in the size of the extracellular space. *Exp. Brain Res.* 46:73–84.

Dietzel, I., U. Heinemann, and H. D. Lux. 1989. Relations between slow extracellular potential changes, glial potassium buffering, and electrolyte and cellular volume changes during neuronal hyperactivity in cat brain. *Glia.* 2:25–44.

Eberhardt, W., and A. Reichenbach. 1987. Spatial buffering of potassium by retinal Müller (glial) cells of various morphologies calculated by a model. *Neuroscience.* 22:687–696.

Gardner-Medwin, A. R. 1983a. A study of the mechanisms by which potassium moves through brain tissue in the rat. *J. Physiol. (Lond.).* 335:353–374.

Gardner-Medwin, A. R. 1983b. Analysis of potassium dynamics in mammalian brain tissue. *J. Physiol. (Lond.).* 335:393–426.

Gardner-Medwin, A. R. 1986. A new framework for assessment of potassium-buffering mechanisms. *Ann. N.Y. Acad. Sci.* 481:287–302.

Gardner-Medwin, A. R., J. A. Coles, and M. Tsacopoulos. 1981. Clearance of extracellular potassium: evidence for spatial buffering by glial cells in the retina of the drone. *Brain Res.* 209:452–457.

Gardner-Medwin, A. R., and C. Nicholson. 1983. Changes of extracellular potassium activity induced by electric current through brain tissue in the rat. *J. Physiol. (Lond.).* 335:375–392.

Immel, J., and H. Steinberg. 1986. Spatial buffering of K^+ by the retinal pigment epithelium. *J. Neurosci.* 6:3197–3204.

Karwoski, C. J., H. K. Lu, and E. A. Newman. 1989. Spatial buffering of light-evoked potassium increases by retinal Müller (glial) cells. *Science.* 244:578–580.

Kettenmann, H., U. Sonnhof, and M. Schachner. 1983. Exclusive potassium dependence of the membrane potential in cultured mouse oligodendrocytes. *J. Neurosci.* 3:500–505.

Kuffler, S. W., J. G. Nicholls, and R. K. Orkand. 1966. Physiological properties of glial cells in the central nervous system of amphibia. *J. Neurophysiol.* 29:768–787.

Lehmenkühler, A., E. Syková, J. Svoboda, K. Zilles, and C. Nicholson. 1993. Extracellular space parameters in the rat neocortex and subcortical white matter during postnatal development determined by diffusion analysis. *Neuroscience.* 55:339–351.

Lothman, E. W., and G. G. Somjen. 1975. Extracellular potassium activity, intracellular and extracellular potential responses in the spinal cord. *J. Physiol. (Lond.).* 252:115–136.

Luby-Phelps, K., D. L. Taylor, and F. Lanni. 1986. Probing the structure of cytoplasm. *J. Cell Biol.* 102:2015–2022.

Mi, H., T. J. Deerinck, M. Jones, M. H. Ellisman, and T. L. Schwarz. 1996. Inwardly rectifying K^+ channels that may participate in K^+ buffering are localized in microvilli of Schwann cells. *J. Neurosci.* 16:2421–2429.

Newman, E. A. 1984. Regional specialization of retina glial cell membrane. *Nature.* 309:155–157.

Newman, E. A. 1985. Membrane physiology of retinal glial (Müller) cells. *J. Neurosci.* 5:2225–2239.

Newman, E. A. 1986. High potassium conductance in astrocyte endfeet. *Science.* 233:453–454.

Newman, E. A. 1993. Inward-rectifying potassium channels in retinal glial (Müller) cells. *J. Neurosci.* 13:3333–3345.

Newman, E. A., and L. L. Odette. 1984. Model of electroretinogram b-wave generation: a test of the K^+ hypothesis. *J. Neurophysiol.* 51:164–182.

Nicholson, C., and J. M. Phillips. 1981. Ion diffusion modified by tortuosity and volume fraction in the extracellular microenvironment of the rat cerebellum. *J. Physiol. (Lond.).* 321:225–257.

Nicholson, C., and E. Syková. 1988. Extracellular space structure revealed by diffusion analysis. *Trends Neurosci.* 21:207–215.

Oakley, B., II, B. J. Katz, Z. Xu, and J. Zheng. 1992. Spatial buffering of extracellular potassium by Müller (glial) cells in the toad retina. *Exp. Eye Res.* 55:539–550.

Odette, L. L., and E. A. Newman. 1988. Model of potassium dynamics in the central nervous system. *Glia.* 1:198–210.

Orkand, R. K., J. G. Nicholls, and A. R. Kuffler. 1966. Effect of nerve impulses on the membrane potential of glial cells in the central nervous system of amphibia. *J. Neurophysiol.* 29:788–806.

Paulson, O. B., and E. A. Newman. 1987. Does the release of potassium from astrocyte endfeet regulate blood flow? *Science.* 237:896–898.

Pilgrim, C. H., I. Reisert, and D. Grab. 1982. Volume densities and specific surfaces of neuronal and glial tissue elements in the rat supraoptic nucleus. *J. Comp. Neurol.* 211:427–431.

Ransom, B. R., C. L. Yamate, and B. W. Connors. 1985. Activity-dependent shrinkage of extracellular space in rat optical nerve: a developmental study. *J. Neurosci.* 5:532–535.

Reichenbach, A., and S. R. Robinson. 1995. Ependymoglia and ependymoglia-like cells. *In* Neuroglia. H. Kettenmann and B. R. Ransom, editors. Oxford University Press, New York. 58–96.

Skatchkov, S. N., J. Krušek, A. Reichenbach, and R. A. Orkand. 1999. Potassium buffering by Müller cells isolated from the center and periphery of the frog retina. *Glia.* 27:171–180.

Skatchkov, S. N., L. Vyklicky, and R. A. Orkand. 1995. Potassium currents in endfeet of isolated Müller cells from the frog retina. *Glia.* 15:54–64.

Sontheimer, H. 1994. Voltage-dependent ion channels in glial cells. *Glia.* 11:156–172.

Syková, E. 1983. Extracellular K^+ accumulation in the central nervous system. *Prog. Biophys. Mol. Biol.* 42:135–189.

Walz, W. 1989. Role of glia cells in the regulation of the brain ion microenvironment. *Prog. Neurobiol.* 33:309–333.